Remote Sensing of Environment 260 (2021) 112444

Contents lists available at ScienceDirect

Remote Sensing of Environment

journal homepage: www.elsevier.com/locate/rse

Performance of Ocean Colour Chlorophyll *a* algorithms for Sentinel-3 OLCI, MODIS-Aqua and Suomi-VIIRS in open-ocean waters of the Atlantic

Gavin H. Tilstone [a,*], Silvia Pardo [a], Giorgio Dall'Olmo [a,b], Robert J.W. Brewin [c], Francesco Nencioli [a,1], David Dessailly [d], Ewa Kwiatkowska [d], Tania Casal [e], Craig Donlon [e]

[a] PML - Plymouth Marine Laboratory, Prospect Place, The Hoe, Plymouth PL1 3DH, UK
[b] National Centre for Earth Observation, Plymouth PL1 3DH, UK
[c] Centre for Geography and Environmental Science, College of Life and Environmental Sciences, University of Exeter, Penryn Campus, Penryn TR10 9FE, UK
[d] EUMETSAT, Eumetsat Allee 1, 64295 Darmstadt, Germany
[e] European Space Agency (ESA) - European Space Research and Technology Centre (ESTEC), Keplerlaan 1, Noordwijk, Netherlands

ARTICLE INFO

Editor: Menghua Wang

Keywords:
Sentinel-3
OLCI
Validation
Atmospheric correction
Atlantic Ocean
MODIS-Aqua
Suomi-VIIRS
Sentinel-3A and 3B Tandem Phase
Chlorophyll *a*

ABSTRACT

The proxy for phytoplankton biomass, Chlorophyll *a* (Chl *a*), is an important variable to assess the health and state of the oceans which are under increasing anthropogenic pressures. Prior to the operational use of satellite ocean-colour Chl *a* to monitor the oceans, rigorous assessments of algorithm performance are necessary to select the most suitable products. Due to their inaccessibility, the oligotrophic open-ocean gyres are under-sampled and therefore under-represented in global *in situ* data sets. The Atlantic Meridional Transect (AMT) campaigns fill the sampling gap in Atlantic oligotrophic waters. In-water underway spectrophotometric data were collected on three AMT field campaigns in 2016, 2017 and 2018 to assess the performance of Sentinel-3A (S3-A) and Sentinel-3B (S3-B) Ocean and Land Colour Instrument (OLCI) products. Three Chl *a* algorithms for OLCI were compared: Processing baseline (pb) 2, which uses the ocean colour 4 band ratio algorithm (OC4Me); pb 3 (OL_L2M.003.00) which uses OC4Me and a colour index (CI); and POLYMER v4.8 which models atmosphere and water reflectance and retrieves Chl *a* as a part of its spectral matching inversion. The POLYMER Chl *a* for S-3A OLCI performed best. The S-3A OLCI pb 2 tended to under-estimate Chl *a* especially at low concentrations, while the updated OL_L2M.003.00 provided significant improvements at low concentrations. OLCI data were also compared to MODIS-Aqua (R2018 processing) and Suomi-NPP VIIRS standard products. MODIS-Aqua exhibited good performance similar to OLCI POLYMER whereas Suomi-NPP VIIRS exhibited a slight under-estimate at higher Chl *a* values. The reasons for the differences were that S-3A OLCI pb 2 R_{rs} were over-estimated at blue bands which caused the under-estimate in Chl *a*. There were also some artefacts in the R_{rs} spectral shape of VIIRS which caused Chl *a* to be under-estimated at values >0.1 mg m^{-3}. In addition, using *in situ* R_{rs} to compute Chl *a* with OC4Me we found a bias of 25% for these waters, related to the implementation of the OC4ME algorithm for S-3A OLCI. By comparison, the updated OLCI processor OL_L2M.003.00 significantly improved the Chl *a* retrievals at lower concentrations corresponding to the AMT measurements. S-3A and S-3B OLCI Chl *a* products were also compared during the Sentinel-3 mission tandem phase (the period when S-3A and S-3B were flying 30 sec apart along the same orbit). Both S-3A and S-3B OLCI pb 2 under-estimated Chl *a* especially at low values and the trend was greater for S-3A compared to S-3B. The performance of OLCI was improved by using either OL_L2M.003.00 or POLYMER Chl *a*. Analysis of coincident satellite images for S-3A OLCI, MODIS-Aqua and VIIRS as composites and over large areas illustrated that OLCI POLYMER gave the highest Chl *a* concentrations and percentage (%) coverage over the north and south Atlantic gyres, and OLCI pb 2 produced the lowest Chl *a* and % coverage.

* Corresponding author.
E-mail address: ghti@pml.ac.uk (G.H. Tilstone).
[1] Present address: Collecte Localisation Satellites, Parc Technologique du Canal, 11 Rue Hermès, 31,520, Ramonville-Saint-Agnes, France.

https://doi.org/10.1016/j.rse.2021.112444
Received 16 August 2020; Received in revised form 2 April 2021; Accepted 6 April 2021

1. Introduction

Studying Chlorophyll *a* (Chl *a*), a proxy of phytoplankton biomass, is fundamental to understanding the role that phytoplankton play in marine biogeochemistry, including the carbon cycle, the flow of energy through the trophic food web and climate feedback (Groom et al., 2019; Werdell et al., 2018). Large scale spatial and temporal patterns in Chl *a* can be obtained from ocean-colour satellite remote sensing, which can undoubtedly aid our understanding of biogeochemical cycles in the ocean (Chang et al., 2015; Siegel et al., 2014). The study of Chl *a* from satellite started with the first experimental Ocean Colour (OC) instrument in 1978, the Coastal Zone Colour Scanner (CZCS). Since 1997, a succession of ocean colour satellites have been launched, mainly by the National Aeronautics and Space Administration (NASA) and European Space Agency (ESA), and also from Indian Space Research Organisation, China National Space Agency and geostationary OC satellites launched by the Korean Ocean Satellite Centre and Japanese Meteorological Agency. These OC missions have provided data at an unprecedented frequency, both in time and space, to enable synoptic tracking of changes in phytoplankton biomass across the world's oceans, which had not previously been possible (Blondeau-Patissier et al., 2014). The global ocean-colour data record is now more than twenty years old and has provided insight into recent global trends in Chl *a*, showing that due to climate change, Chl *a* is decreasing in some parts of the ocean and increasing in other areas (Gregg et al., 2017; Martinez et al., 2009; Dutkiewicz et al., 2019; Siegel and Franz, 2010). The recent Copernicus Sentinel mission was launched in 2015 and will provide a further two decades of ocean colour data (Donlon et al., 2012).

1.1. Measurement protocols for assessing Ocean Colour products

At the launch of SeaWiFS, the accepted measurement protocol for the determination of *in situ* Chl *a* for satellite validation was either High Performance Liquid Chromatography (HPLC) or spectrophotometric measurements (Mueller, 2000). Based on this, NASA then assembled a comprehensive *in situ* data base of Chl *a* and other optical properties, which led to the formation of SeaWiFS bio-Optical Archive and Storage System (SeaBASS) and NASA bio-Optical Marine Algorithm Dataset (NOMAD) (Werdell and Bailey, 2005). After more than 20 years using these protocols, the number of co-incident satellite and *in situ* Chl *a* measurements are still low compared with other ocean variables like temperature. SeaBASS and NOMAD databases also have a disproportionate amount of high Chl *a* data from coastal and shelf regions where concentrations are generally >0.1 mg m^{-3} (Brewin et al., 2016). When these data are used to construct Chl *a* algorithms, the large errors associated with high *in situ* Chl *a* data inflate the overall error calculated by the algorithm, unless the bias in the distribution of data is accounted for (Moore et al., 2009).

To increase the number of match-ups obtained from remote areas, a recent revision of these satellite validation protocols has resulted in the development of underway methods to measure Chl *a* (IOCCG, 2018). The technique is based on inherent optical property measurements of sea surface particles using ship based flow-through systems (Dall'Olmo et al., 2009; Dall'Olmo et al., 2012; Koponen et al., 2007; Slade et al., 2010; Westberry et al., 2010). Field campaigns such as the Atlantic Meridional Transect (AMT), which was utilised during the NASA SeaWiFS era for the development of the OC4 algorithm (O'Reilly et al., 1998), offer an opportunity to deploy flow-through systems for the validation of algorithms in open-ocean, oligotrophic waters of the Atlantic Ocean.

1.2. Accuracy assessment of Sentinel-3 OLCI data

Comprehensive comparisons of satellite data with field measurements are fundamental for assessing the accuracy of satellite missions (McClain et al., 2004), due to a multitude of uncertainties, mismatches, and sources of error. Validation of satellite R_{rs} and L_w requires accurate and comprehensive *in situ* datasets covering a wide dynamic range of water properties, which take a significant amount of time and resources to collect (Barnes et al., 2019).

S-3A OLCI was launched in February 2016, followed by the S-3B mission in April 2018. OLCI provides global daily ocean colour images at 300 m resolution (Donlon et al., 2012) and is complemented by the use of Sentinel-2 MSI to detect the Chl *a* concentration in bays and estuaries at a resolution of 10–100 m (Drusch et al., 2012). Of the few papers that have been published to date on the accuracy of S-3 OLCI ocean colour products, all have focused on coastal waters. Zibordi et al. (2018) reported a systematic underestimation of OLCI L_w in blue and red spectral regions. They highlighted the difficulty in separating the radiance signal that comes from water and atmosphere. For the atmospheric signal, this can lead to errors in the determination of aerosol load and type, which in turn may trigger a bias or poor performance of the bright pixel atmospheric correction (Moore et al., 2017). The ocean colour signal is a small component (<10%) of the satellite-detected top-of-atmosphere (TOA) radiance and most of the signal comes from atmospheric scattered light. An important means of improving satellite estimates of Chl *a* is through the development of accurate AC schemes that decipher the water radiance or reflectance (Wang et al., 2009). Mograne et al. (2019) therefore recently assessed five AC models for OLCI in the optically complex French coastal waters. They found that the most accurate AC models for these waters are POLYMER and the Case 2 regional coast colour neural network AC (C2R-CC), which for R_{rs}(412) are accurate to 24% and 33%, respectively. Giannini et al. (2021) also found in coastal waters of the northeast Pacific, that OLCI POLYMER provided more accurate Chl *a* and TSM compared with different versions of C2R-CC, though the RPD for POLYMER was still high. Li et al. (2019) evaluated S-3A OLCI, MODIS-Aqua and the Suomi National Polar-orbiting Partnership (NPP) Visible Infra-red Imaging Radiometer Suite (VIIRS) R_{rs} products in open-ocean and coastal waters of the China Sea and reported that the OLCI products are comparable to those of MODIS-Aqua. The average percentage difference (APD) in R_{rs} was lowest at 490 nm (18%), and highest at 754 nm (79%). In addition, OLCI R_{rs} in the open ocean were higher than the *in situ* values, whereas in coastal waters they were lower. In the Arctic waters of the Fram Strait, Liu et al. (2018) found that MODIS-Aqua and OLCI band ratio Chl *a* plus the OLCI C2R-CC product showed promising results. The OLCI POLYMER AC model provided the most reliable Chl *a* estimates.

The objective of this paper is to firstly assess the accuracy of the S-3A OLCI standard (pb 2) Chl *a* product, secondly to compare this with other Chl *a* products available for S-3A (both OL_L2M.003.00 and POLYMER) and also to compare these with MODIS-Aqua and Suomi-VIIRS R2018 Chl *a* products. The performance of S-3A and S-3B OLCI Chl *a* products during the satellites tandem phase are also assessed. This is the first study to date, on the validation of OLCI Chl *a* products in oligotrophic marine waters and the recently released (February 2021) OL_L2M.003.00 products.

2. Methods

2.1. Study area characteristics and sampling regime

The AMT undertakes transects between the UK and the South Atlantic, on NERC research ships during their annual voyage to the Southern Ocean. The transect covers >12,000 km, sampling a wide range of environmental conditions on the 40 day passage. *In situ* data from three AMT campaigns were used: AMT26 from 20th September to 04th November 2016; AMT27 from 21st September to 05th November 2017; and AMT28 from 23rd September to 30th October 2018. All campaigns followed a similar transect between 50°N and 50°S (Fig. 1). AMT26 and AMT28 were undertaken on board the Royal Research Ship (*RRS) James Clark Ross* and AMT27 was on *RRS Discovery*.

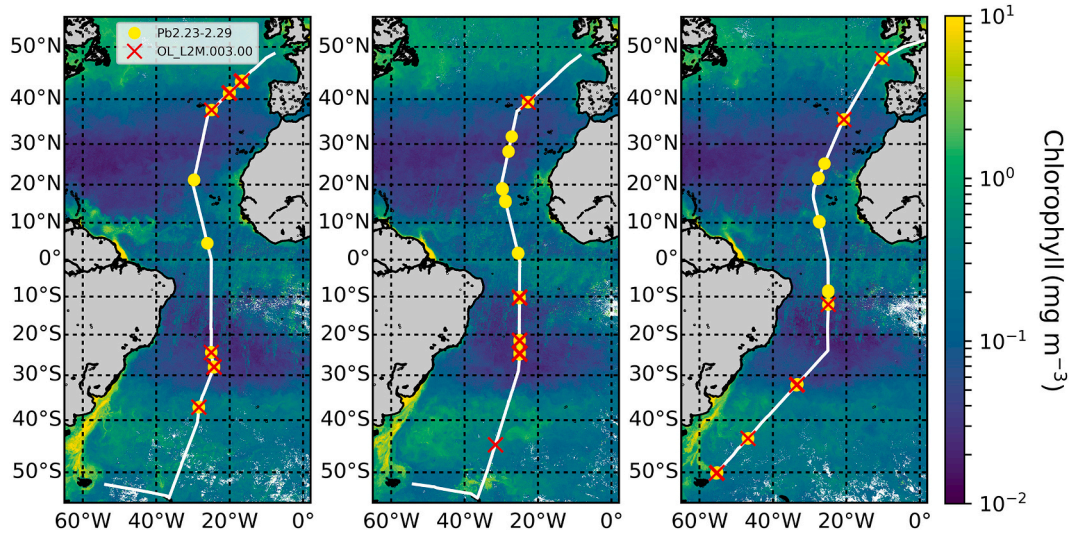

Fig. 1. Station maps of (a.) AMT26 (September–October 2016), (b.) AMT27 (September–October 2017) and (c.) AMT28 (September–October 2018) superimposed on Sentinel-3 OLCI Chlorophyll-*a* composite images for each campaign. The white line is the campaign track; the yellow points indicate the match-ups obtained with OLCI-A Chl *a* pb 2.23 and 2.29 for each campaign; the red crosses (some of which are coincident with the yellow points) indicate the match-ups obtained with OLCI-A Chl *a* OL_L2M.003.00; the Chlorophyll-*a* colour scale is given on the right hand axis of each plot. (For interpretation of the references to colour in this figure legend, the reader is referred to the web version of this article.)

2.2. Discrete measurements of Chlorophyll-a

Water samples were taken from an underway flow-through optical system and from Niskin bottle rosettes deployed with a Seabird Conductivity-Temperature-Depth (CTD) sampling device. During each AMT campaign, between three and six underway samples were collected each day from 04:00 to 22:00 local time. For CTD samples, surface water was collected using 20 L Niskin bottles at 12:00 local time coincident with S-3 over-passes. For both underway and CTD samples, between 1 and 6 L of seawater were filtered onto Whatman glass fibre filters (pore size of 0.7 μm), transferred to Cryovials and stored immediately in liquid nitrogen. After each AMT campaign, High Performance Liquid Chromatography (HPLC) was then used to determine Total Chl *a* (estimated from the sum of monovinyl Chl *a*, divinyl Chl *a*, chlorophyllide *a*). Phytoplankton pigments were extracted into 2 mL 100% acetone and using an ultrasonic probe (35 s, 50 W). Extracts were centrifuged to remove filter and cell debris (3 min at 20 x g) and analyzed by HPLC using a reversed phase C8 column and gradient elution (Barlow et al., 1997) on an Agilent 1100 Series system with chilled auto-sampler (4 °C) and photodiode array detection (Agilent Technologies). The HPLC system was calibrated using a suite of standards (DHI, Water and Environment, Denmark) and pigments in the samples were identified using photodiode array spectroscopy spectral match procedures (Jeffrey et al., 1997). Chl *a* concentrations were calculated using response factors from the respective calibration standard (DHI). The discrete HPLC Chl *a* concentrations were only used to calibrate the underway spectrophotometric measurements, rather than for the purpose of satellite validation.

2.3. Underway spectrophotometric measurements of Chlorophyll a

The underway spectrophotometric Chl *a* measurements were used to assess satellite ocean-colour product performance. On all campaigns, absorption-attenuation instruments were plumbed into the clean flow-through system of the ship, which provides seawater from a depth of ~6 m beneath the hull. The method of determining Chl *a* using the underway spectrophotometry is given in detail in Dall'Olmo et al. (2009). In brief, the seawater was first passed through a debubbler (Vortex), then through the WETLabs ACS (hyperspectral data 400–750 nm, 5 nm spectral resolution, 15 nm band pass) or AC9 (multispectral at 9 wavelength bands) to determine absorption coefficients of particulate matter ($a_p(\lambda)$). The seawater was also periodically passed through a Cole Parmer 0.2-μm cartridge filter (for 10 min every hr) and the 0.2-μm filtered absorption was used as a baseline for the determining particle absorption (Dall'Olmo et al., 2012; Slade et al., 2010). These data were then converted into 1-min median bins. With an average ship speed of ~18 km h^{-1}, each 1-min binned median represents approximately 0.3 km of the transect. For AMT28, measurements from both ACS and AC9 were used and the protocol of Dall'Olmo et al. (2012) was deployed to bridge Chl *a* measurements between the two instruments. For all AMT campaigns, $a_p(\lambda)$ data at 650, 676 and 715 nm were used to estimate Chl *a* concentrations using the line height method of Boss et al. (2007), as follows:

$$Chl\ a_{ACSn} = \left[a_p(676) - \frac{39}{65}a_p(650) - \frac{26}{65}a_p(715)\right] \Big/ 0.014 \quad (1)$$

where $Chl\ a_{ACSn}$ is the estimate of Chl *a* from ACS or AC9 (hereafter referred to as ACS Chl *a*) and 0.014 m^2 mg^{-1} Chl *a* is a typical estimate of Chl *a* specific absorption at 676 nm. Estimates of ACS Chl *a* were de-biased by comparing them to HPLC Chl *a* using the median relative residuals (Graban et al., 2020). This bias is usually due to variation in instrument characteristics and calibration which are normally small (~10%). The uncertainty of the de-biased ACS Chl *a* was estimated using the standard deviation of the relative residuals (σ_{rel}) resulting by comparing it with the HPLC data. σ_{rel} was 7.7%, 12.5% and 4.4% for AMT26, 27 and 28, respectively. We used the average of these values (8.2%) as an estimate of the typical relative uncertainty of the de-biased ACS Chl *a*. Eq. (1) was then used to reconstruct Chl *a* for all $a_p(\lambda)$ data, resulting in 39,274 1-min binned Chl *a* samples for AMT26, 35,796 for AMT27 and 22,294 for AMT28. A comparison of Chl *a* estimated from the absorption-attenuation instruments and the corresponding HPLC Chl *a* data for each field campaign are given in Fig. 2. *In situ* ACS Chl *a* were averaged in $\log_{10}$ space over a 20-min period centred on the time the discrete HPLC water samples were collected (± 10 min).

2.4. Underway radiometric sampling of remote sensing reflectance

A radiometric measurement system consisting of three hyperspectral spectroradiometers was deployed on all three AMT cruises. Two of the

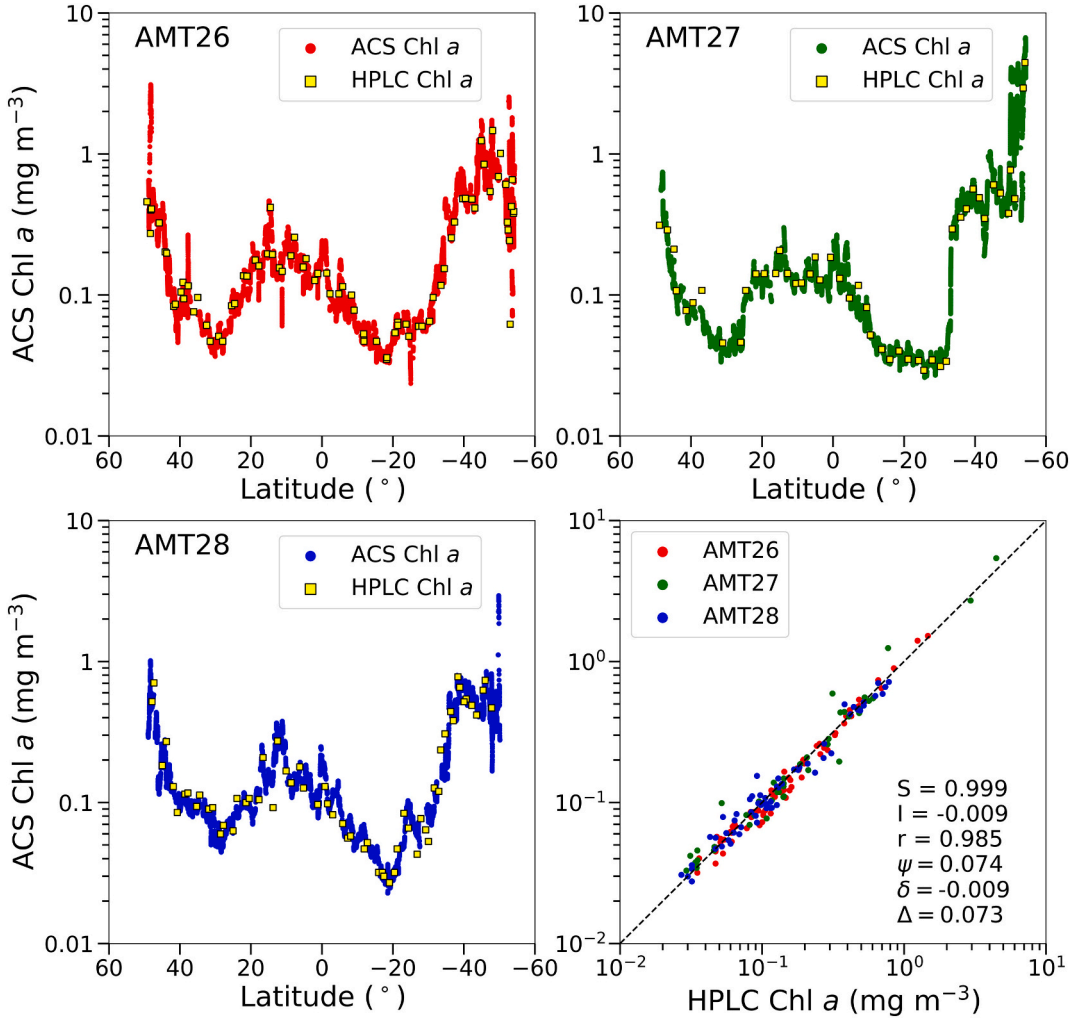

Fig. 2. Variability in ACS Chl *a* by latitude for (a.) AMT26, (b.) 27 and (c.) 28, (d.) comparison of HPLC against ACS Chl *a*. The statistical metrics given in (d.) are defined in Section *2.3. 'Match-up procedure'*.

radiometers measure radiance (using a field of view of 6°); one measures sky radiance (L_{sky}), the second measures total above-water upwelling radiance (L_t). The third instrument measures downwelling irradiance (E_d). L_{sky}, L_t and E_d were measured from 350 to 950 nm at each 3.3 nm interval using a spectral width of 10 nm. The integration time varies from 4 ms to 8 s and is adjusted automatically based on the ambient light conditions. A two-axis tilt sensor is incorporated with the E_d sensor. A steel frame was bolted to the bow of the ship into which the radiance sensors were fixed so that the L_{sky} sensor had a viewing zenith angle (θ) of 40° and the L_t θ was 140°. The steel frame was positioned so that the sensors were out of the ship's shadow and only viewed the sea surface, which on *RRS James Clark Ross* (AMT26 & 28) is approximately 8 m and on *RRS Discovery* (AMT29) is 18 m above the sea surface. To avoid optical interference from surrounding structures, the E_d sensor was mounted separately on the meteorological mast, which is the highest point on the ship. Details of the data processing are given in Tilstone et al. (2020). In brief, each sensor has a dark shutter that periodically closes to provide dark counts which were subtracted from the light measurements from each sensor at each wavelength. Pre- and post-campaign calibration coefficients were applied to the extracted raw data files, which were then interpolated to 2 nm intervals. R_{rs} is the ratio of the water leaving radiance (L_w) to the above-water downwelling irradiance E_d and was computed from:

$$R_{rs}(\theta,\theta_0,\Delta\phi,\lambda)=\frac{L_w(\theta,\theta_0,\Delta\phi,\lambda)}{E_d(0^+,\lambda)}. \quad (2)$$

L_w was computed from L_t and the removal of sky glint (L_{sky}) effects following:

$$L_w(\theta,\theta_0,\Delta\phi,\lambda)=L_t(\theta,\theta_0,\Delta\phi,\lambda)-\rho(\theta,\theta_0,\Delta\phi,U_{10})L_{sky}(\theta',\theta_0,\Delta\phi,\lambda), \quad (3)$$

The measurement geometry of the sensors is accounted for by the sea viewing zenith angle (θ), sun zenith angle (θ_0) and the relative azimuth angle between the sun and sensors (Δϕ). The term $\rho(\theta,\theta_0,\Delta\phi,U_{10})$ accounts for skylight reflected at the air-water interface and is parameterised as a function of wind speed at 10 m above the sea surface (U_{10}) and of the sun-sensor geometry (Mobley, 1999). A near-infra red (NIR) correction was applied for these open-ocean data, in which R_{rs}(750) was subtracted from each R_{rs} spectrum following Hooker et al. (2002). The data were filtered and quality control checked by eliminating measurements with a tilt >±5°, sun glint following Hooker et al. (2002), high solar zenith angles >80° and relative azimuth angles >50° and 170°. To cross-check the performance of OC4Me, the underway R_{rs} were used to run OC4Me to generate Chl *a* concentrations, which were compared against ACS Chl *a*.

Table 1
Functional form of S-3 OLCI, MODIS-Aqua and Suomi-VIIRS Chl *a* algorithms.

Algorithm	Reference	Functional form
OCx	See below	$log10(Chl\ a) = a0 + bR + cR^2 + dR^3 + eR^4$
S-3 OLCI OC4Me + CI	Morel and Antoine (2011) Cazzaniga and Kwiatkowska (2018)	*Chl a* from OCx with the largest reflectance ratio (R) from: $R = log_{10}\left\{max\left[\left(\frac{R_{rs}(443)}{R_{rs}(560)}\right)\left(\frac{R_{rs}(490)}{R_{rs}(560)}\right),\left(\frac{R_{rs}(510)}{R_{rs}(560)}\right)\right]\right\}$ OCx coefficients are: $a0 = 0.3255$; $b = -2.7677$; $c = 2.4409$; $d = -1.12259$; $e = 0.5683$. $CI = R_{rs}(560) - \left[R_{rs}(442.5) + \frac{560-442.5}{665-442.5}R_{rs}(665) - R_{rs}(442.5)\right]$ $Log_{10}(chl_{CI}) = b\ CI + a$ where b = −0.5379 and a = 180.9642.
S-3 OLCI POLYMER v4.8	Steinmetz et al. (2011)	$T_0(\lambda)c_0 + c_1\lambda^{-1} + c_2\lambda^{-4} \approx \rho'(\lambda) - t(\lambda)\rho^{+}_{wmod}([Chl]_i b_{bNC,\ i}, \lambda)$ Where $T_0(\lambda)$ is the transmission factor which accounts for beam attenuation due to rayleigh scattering, c_0, $c_1$and c_2 are coefficients for the residue of sun-glint, the aerosol scattering and the coupling, ρ' is the sea surface reflectance corrected for wind speed, residue sun-glint and aerosol scattering, ρ^{+}_{wmod} is the modelled water reflectance above the water-air interface, *Chl* is the chlorophyll concentration, b_{bNC} is the backscattering coefficient of non-covarying particles.
MODIS-Aqua (OC3 + CI) and Suomi-VIIRS (OC3V + CI)	Hu et al., 2012 O'Reilly et al. (2000)	At *Chl a* concentrations <0.15 mg m^{-3} the CI algorithm used is: $CI = R_{rs}(\lambda_{green}) - [R_{rs}(\lambda_{blue}) + (\lambda_{green} - (\lambda_{blue})/(\lambda_{red} - (\lambda_{blue}) * (R_{rs}(\lambda_{red}) - R_{rs}((\lambda_{blue}))]$ where λ_{blue}, λ_{green} and λ_{red} are the instrument-specific wavelengths For MODIS-Aqua these are 443, 547 and 667 nm, respectively. For Suomi-VIIRS, these are 443, 550 and 670 nm. At *Chl a* concentrations >0.2 mg m^{-3} OC3 with the R ratio to the nearest corresponding band is used: $R = log_{10}\left\{max\left[\left(\frac{R_{rs}(443)}{R_{rs}(547)}\right),\left(\frac{R_{rs}(488)}{R_{rs}(547)}\right)\right]\right\}$ For MODIS-Aqua, OC3 coefficients are: $a0 = 0.2424$; $b = -2.7423$; $c = 1.8017$; $d = 0.0015$; $e = -1.228$. For Suomi-VIIRS, OC3V coefficients are $a_0 = 0.2228$, $b = -2.4683$, $c = 1.5867$, $d = -0.4275$, $e = -0.7768$.

2.5. Satellite data processing and algorithms

S-3 OLCI passes were firstly acquired within ±1 h along the AMT26, AMT27 and AMT28 campaign tracks. The corresponding S-3 OLCI full resolution data level 1 and 2 products were downloaded from the EUMETSAT Data Centre and Copernicus Online Data Access (CODA) portals respectively. S-3A OLCI processing baseline (pb) 2.23 data was used concurrent with *in situ* measurements taken on AMT26 and AMT27 and S-3A OLCI pb 2.29 and S-3B OLCI pb 1.30 data were used for AMT28. The atmospheric correction implemented for these level 2 products is described in Antoine (2010). For S-3A OLCI, there is no difference between pb 2.23 and 2.29 in the level 2 processing, yet there are small changes at the level 1 processing primarily accounting for improvements in pixel geo-location. For S-3A OLCI pb2.23–2.29 and S-3B OLCI pb1.30, the standard Case 1 Chl *a* water type algorithm is applied (OC4Me; Morel and Maritorena, 2001; Morel and Antoine, 2011), which is a fourth-order polynomial that utilises a maximum R_{rs} ratio based on 442, 490 and 560 nm using the equation given in Table 1. The algorithm switches between $R_{rs}(442)$ / $R_{rs}(560)$ and $R_{rs}(490)$ / $R_{rs}(560)$ at 0.53 mg m^{-3} Chl *a* and between $R_{rs}(490)$ / $R_{rs}(560)$ and $R_{rs}(510)$ / $R_{rs}(560)$ at 2.23 mg m^{-3} Chl *a*. In addition, the recent 3rd reprocessing of S-3A and S-3B OLCI level 2 products (OL_L2M.003.00) were also downloaded. Improvements to OL_L2M.003.00 include updated system vicarious calibration gains (https://www.eumetsat.int/ocean-colour-system-vicarious-calibration-tool), bright pixel correction (https://www.eumetsat.int/OC-BPC), cloud masking (Wang and Shi, 2006) and user flag recommendations (https://www.eumetsat.int/sentinel-3), whitecap correction (Stramska and Petelski, 2003; Frouin et al., 1996), as well as the implementation of a colour index (CI) algorithm for low Chl *a* waters (Cazzaniga and Kwiatkowska, 2018; Hu et al., 2012), the details of which are given in Table 1. S-3A OLCI OL_L2M.003.00 implements CI at $\frac{R_{rs}(443)}{R_{rs}(560)}$ ratios <3 and at ratios >4 it implements OC4Me. A blended weighted average Chl *a* concentration is applied to data between the ratio of 3 and 4. OLCI level 1 passes were also processed to level 2 using the AC processor POLYMER v4.8, which is an atmospheric correction procedure, originally developed for MERIS, that also retrieves ocean-colour parameters. It employs an iterative coupled ocean-atmosphere algorithm where the atmosphere contribution to the top-of-atmosphere reflectance is modelled as a polynomial (Steinmetz et al., 2011). The bio-optical water reflectance model component is based on the Chl *a* concentration and the backscattering coefficient of non-covarying particles. The reflectance spectra are modelled following Morel (1988) and Morel and Maritorena (2001) and Chl *a* is derived from in water reflectance spectral matching which uses a 2-dimensional optimization based on the log Chl *a* concentration (Loisel and Morel, 1998) and the backscattering coefficient (Table 2).

Each of the AC processors applied to S-3A OLCI data uses a different system vicarious calibration (SVC). The S-3A OLCI pb 2.23–2.29 uses a mix of *in situ* and climatological satellite data to derive visible band gains (S3MPC, 2017). S-3B OLCI pb 1.30 does not apply SVC and the value of 1 for all gains is assumed. The updated OLCI processor OL_L2M.003.00 implements SVC based match-ups with MOBY *in situ* measurements, with four years of matchups for S-3A OLCI and two years for S-3B OLCI (https://www.eumetsat.int/ocean-colour-system-vicarious-calibration-tool). POLYMER uses an *in situ* based SVC designed for ocean-atmosphere coupled algorithms (Steinmetz and Ramon, 2018).

Table 2
Flags used to process each ocean-colour Chl *a* product. If any of the flags listed were raised, data for each product were not included.

Processor	Flags implemented
S-3A OLCI L2 pb 2.23–2.29 (OC4Me) and S-3B OLCI L2 pb 1.30 (OC4Me)	INVALID, LAND, CLOUD, CLOUD AMBIGUOUS, SUSPECT, CLOUD MARGIN, SNOW_ICE, HISOLZEN, SATURATED, HIGHGLINT, WHITECAPS, AC_FAIL, ANNOT_TAU06
S-3A and S-3B OLCI OL_L2.003.00 (OC4Me + CI)	CLOUD, CLOUD_AMBIGUOUS, CLOUD_MARGIN, INVALID, COSMETIC, SATURATED, SUSPECT, HISOLZEN, HIGHGLINT, SNOW_ICE, AC_FAIL, WHITECAPS, RWNEG_O2, RWNEG_O3, RWNEG_O4, RWNEG_O5, RWNEG_O6, RWNEG_O7, RWNEG_O8, ADJAC.
MODIS-Aqua / Suomi-VIIRS	ATMFAIL, LAND, HIGLINT, HILT, HISATZEN, STRAYLIGHT, CLDICE, COCCOLITH, HISOLZEN, LOWLW, CHLFAIL, NAVWARN, MAXAERITER, ATMWARN, NAVFAIL
S-3 OLCI POLYMER Chl *a*	ATMFAIL, LAND, HIGLINT, HILT, HISATZEN, STRAYLIGHT,
SVC gains applied to OLCI POLYMER v4.8; λ (nm) = gain	400 = 1, 412 = 0.997, 443 = 0.997, 490 = 0.989, 510 = 0.993, 560 = 0.998, 620 = 1, 665 = 1, 754 = 1, 779 = 1, 865 = 1, 1020 = 1 (Mazeran et al., 2020)

Version 4.8 of POLYMER did not originally apply SVC, however we applied the SVC gains to POLYMER that are given in Table 2 following Mazeran et al. (2020). The latest NASA Ocean Colour Reprocessing (R2018.0) for MODIS-Aqua and Suomi-NPP VIIRS passes were acquired within 12 h of the *in situ* underway samples. The corresponding level 2 granules were downloaded at 1 km and 750 m resolution respectively from the NASA Distributed Active Archive Centre through the Ocean Colour Web portal (https://oceancolor.gsfc.nasa.gov). This resulted in 55 passes for MODIS-Aqua and 78 passes for VIIRS. For MODIS-Aqua and VIIRS the NASA chlor_a parameter was used, which deploy the OCx + CI algorithms (Table 1). For MODIS-Aqua and VIIRS OC3 is utilised at Chl *a* concentrations >0.2 mg m^{-3}. Like OC4, OC3 is a band ratio algorithm that uses one of two blue bands with blue-green $R_{rs}(\lambda)$, at 547 nm for MODIS-Aqua and 550 nm for VIIRS, as the denominator (O'Reilly et al., 2000), as shown in Table 1. At Chl *a* concentrations <0.15 mg m^{-3}, both MODIS-Aqua and VIIRS utilise the OCI of Hu et al. (2012) based on the difference in R_{rs} between a green band and red and blue bands (Table 1).

In order to exclude unreliable satellite measurements for each product, a set of recommended quality flags were applied as a mask to each pass. Table 2 lists the processing flags applied for each of the processors. For S-3A OLCI pb2.23–2.29 and S-3B OLCI pb 1.30 additional RWNEG and ANNOT_ABSO_D and ANNOT_MIXR1 are also recommended for the R_{rs} standard products (https://www.eumetsat.int/media/44087), which we did not use. The RWNEG flag is raised for negative water leaving radiance at each band and does not apply to the Chl *a* product as negative water leaving radiances are not used to compute Chl *a* concentrations. The ANNOT flags provide some quality assurance of the atmospheric correction procedure. These have been shown however, to have a significant impact on the analysis of data from open ocean regions and may lead to the exclusion of a large number of *in situ* and satellite match-ups especially in optically complex regions (Zibordi et al., 2018). Once the flags were applied, R_{rs} data from each ocean-colour satellite sensor were used to generate the corresponding Chl *a* product.

To produce the campaign composites and gyre time series, all data were time-averaged (at campaign, weekly and daily levels) and mapped re-gridded to 1 km resolution.

2.6. Match-up procedure

The method used for match-up analysis follows Bailey and Werdell (2006), and was adapted for AMT underway data following Brewin et al. (2016). Ocean colour level 2 data from satellite over-passes within ±1 h of underway measurements were used. The satellite data were extracted from a 3 × 3 pixel box centred on the measurement coordinate and were excluded if the median coefficient of variation (CV) was >0.15 or when there were < 50% of the pixels available (Bailey and Werdell, 2006). Based on the ship speed (~18 km h^{-1}), each 1-min averaged bin represents 0.3 km. From the 3 × 3 pixels, the centre pixel was used for the validation procedure. The *in situ* data (1-min bins) were matched to individual satellite pixels. All *in situ* data within a specific pixel were averaged, so that each match-up has an independent set of *in situ* data and there were no overlapping *in situ* data between match-ups. The validation statistics were computed on the centre pixel, to ensure that each match-up uses an independent satellite pixel. Additionally, the standard deviation around the match-up (from the 3 × 3 box) was computed as an index of the homogeneity of the match-up. Although validation statistics are independent, as each pixel is independent (central pixel of the 3 × 3 box) and used an independent set of *in situ* data, it is noted that the 3 × 3 box may contain overlapping pixels for cases where match-ups are from neighbouring pixels. For these, the standard deviations computed around each match-up (index of homogeneity) will not be entirely independent. These standard deviations

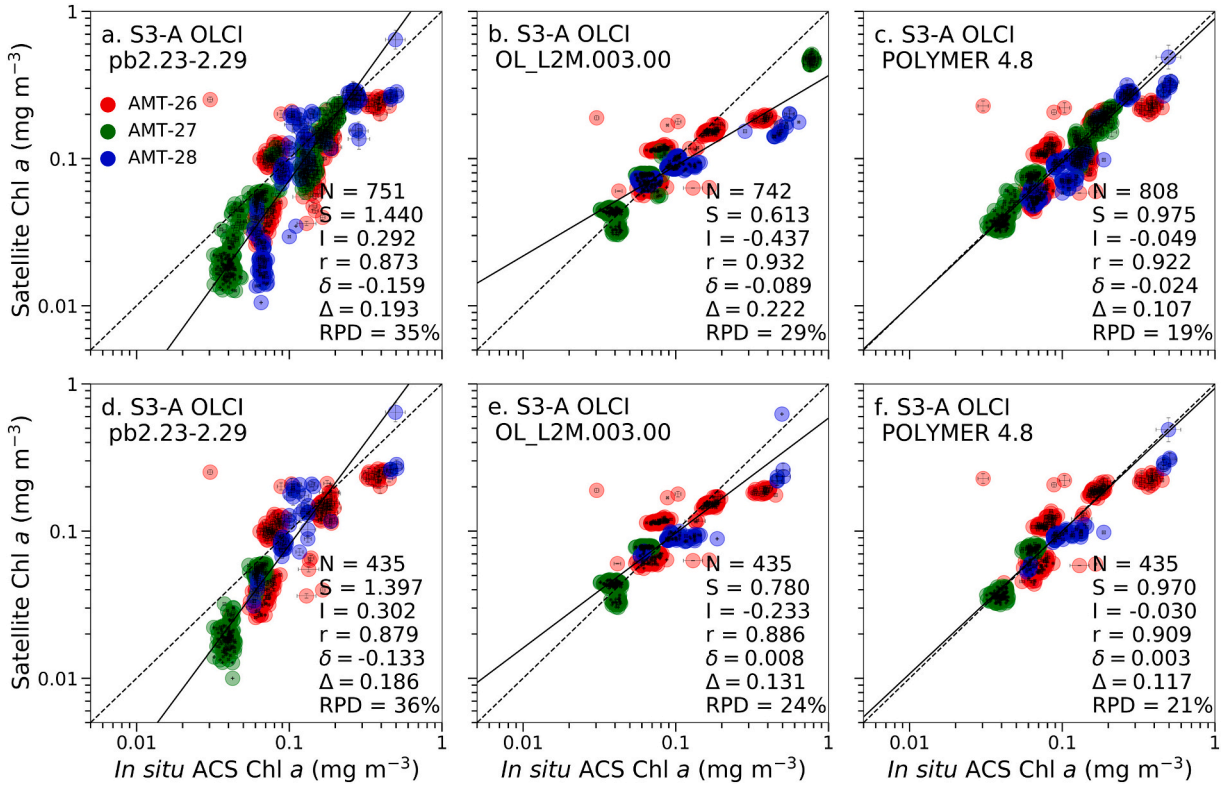

Fig. 3. Scatter plots of *in situ* ACS Chl *a* from AMT26, 27, 28 *versus* (a.) S-3A OLCI Chl *a* pb 2.23–2.29 (OCMe); (b.) S-3A OLCI Chl *a* OL_L2.003.00 (OCMe+CI); (c.) S-3A OLCI Chl *a* POLYMER v4.8, for independent match-ups (d.) S-3A OLCI Chl *a* pb 2.23–2.29 (OCMe); (e.) S-3A OLCI Chl *a* OL_L2.003.00 (OCMe+CI); (f.) S-3A OLCI Chl *a* POLYMER v4.8, for coincident match-ups. The standard deviation of the $\log_{10}$-transformed Chl *a* at each station was calculated to provide the error bars in *in situ* ACS Chl *a* measurements.

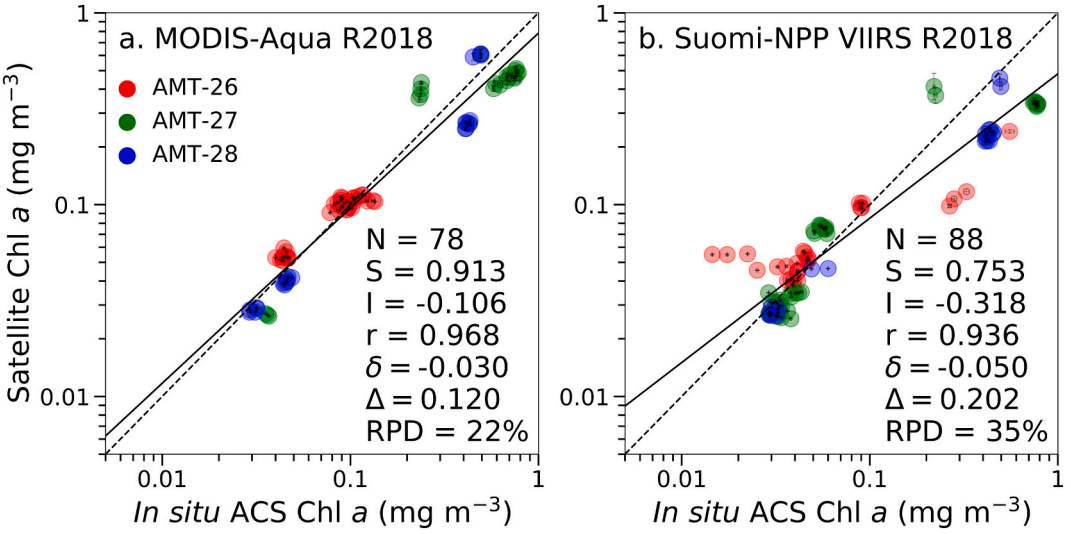

Fig. 4. Scatter plots of *in situ* ACS Chl *a* from AMT26, 27, 28 *versus* (a.) MODIS-Aqua Chl *a*, (b.) VIIRS Chl *a*, for coincident match-ups with S-3A OLCI. (For interpretation of the references to colour in this figure legend, the reader is referred to the web version of this article.)

however, were only used qualitatively in scatter plots, and not formally in the computation of the validation statistics. The standard deviation in the *in situ* data were then calculated within each satellite pixel and plotted as the error bars given in Figs. 3, 4, 6, 7, 9. This method captures a large number of match-ups at very high resolution and is therefore representative of the variability in Chl *a* over both homogenous and heterogeneous surface water conditions, and also of atmospheric conditions.

For S-3A OLCI Chl *a* pb 2.23–2.29, there were 27 satellite images coincident with the *in situ* ACS Chl *a* from the underway system which gave $N = 751$, and for S-3A OLCI Chl *a* OL_L2M.003.00 there were 17 OLCI images which provided $N = 742$ match-ups. Typically, there were ~ 45 pixels in the ensemble of match-ups for each S-3A OLCI image. For OLCI pb 2.23–2.29, the pixels were clustered over an area of 2.6 km^2 with the average number of pixels per image being 29 pixels. By comparison, for OL_L2M.003.00, the pixels were clustered over an area of 3.9 km^2 with an average number of pixels of 43. The differences between OLCI pb 2.23–2.29 and OL_L2M.003.00 arise from the QC flags used (Table 2). For MODIS-Aqua and Suomi-VIIRS there were 11 and 17 images available respectively, coincident with the *in situ* ACS Chl *a*. The differences between the number of match-ups available between S-3A OLCI and the NASA products are due to the flags used (Table 2), the overpass times and the resolution. One MODIS–Aqua pixel for example, is equivalent to 3 × 3 OLCI full resolution pixels. For the same number of images S-3 OLCI will therefore have an order of magnitude higher number of match-ups.

2.7. Statistical metrics

The following statistical metrics were used to evaluate algorithm performance following Brewin et al. (2015b) and Muller et al. (2015): type-II regression slope (S), intercept (I), Pearson correlation coefficient (r), root-mean-square difference (RMSD - Ψ), the bias (δ), bias-corrected root-mean-square error (Δ), and the relative percentage difference (RPD) which was computed with modulus. The S, I, r, Ψ, δ and Δ were computed in $\log_{10}$ space. To facilitate interpretation of these statistical metrics for satellite validation, an S close to one and an intercept I close to zero indicate a good fit between satellite and *in situ* data. Similarly, the higher the r the better the linear consistency between the *in situ* and the satellite observations. S, I and r do not convey information on the distribution of the data around the regression line and outliers which is provided by Ψ, δ and Δ. Ψ is the relative difference between satellite and *in situ* data and is sensitive to the differences around the regression line. Δ is the bias corrected difference between satellite and *in situ* data and is sensitive to any outliers. The δ provides information on the under-estimate or over-estimate of the satellite data compared to the *in situ* data, with a value near zero indicating no systematic difference between the two data sets.

3. Results

3.1. Accuracy assessment of ocean-colour algorithms for OLCI in the Atlantic Ocean

Location of the match-ups between spectrophotometric determined ACS Chl *a* and S-3A OLCI for the three AMT campaigns are given in Fig. 1. Of the 751 match-ups with S-3A OLCI pb 2.23–2.29, over half were in the oligotrophic gyres ($N = 429$). The others were in the mesotrophic equatorial upwelling ($N = 137$), North Atlantic Drift Province ($N = 65$) and the South Sub-tropical Convergence Zone ($N = 9$) (provinces as per Longhurst et al. (1995)). Scatter plots of *in situ* ACS Chl *a* against OLCI Chl *a* from the three different processors for all match-ups obtained (referred as 'independent' hereafter) and for match-ups common to all OLCI processors (referred as 'coincident' hereafter) are given in Fig. 3. The error bars in *in situ* ACS Chl *a* measurements for the x-axis is given as the standard deviation calculated at each match-up pixel. The error bars in the satellite measurement are calculated from the standard deviation over the 3 × 3 pixels centered on each sampling station and thus represent the spatial variability. The error bars in *in situ* ACS Chl *a* were smaller in the low Chl *a* waters of the north and south Atlantic gyre and higher at either end of the Transect and varied from 0.001 mg m^{-3}, at 25.06°N in the north Atlantic gyre to 0.689 mg m^{-3} at 48.08°S in the Southern Sub-tropical Convergence Zone.

For the independent match-ups, S-3A OLCI Chl *a* pb 2.23–2.29 (OC4Me) exhibited a large offset at low and higher (0.3–0.6 mg m^{-3}) Chl *a* concentrations, a high slope, intercept, RMSD and negative bias, resulting in an RPD of 35% (Fig. 3a). S-3A OLCI Chl *a* OL_L2M.003.00 (OC4Me + CI) returned the lowest number of match-ups ($N = 742$), a low slope, high intercept, bias and RMSD resulting in an RPD of 29% (Fig. 3b). For this Chl *a* product, the regression was skewed by a cluster of points associated with match-ups in 2017 and 2018 between 33°S and 44°S in which OLCI under-estimated Chl *a* over the ACS Chl *a* range from 0.1 to 1.0 mg m^{-3}. The number of match-ups for OLCI POLYMER Chl *a* were the highest ($N = 808$), and it performed best, with a slope and r close to 1 and the lowest intercept, bias and RMSD and an RPD of 19% (Fig. 3c). When the same matchups were used for each processor ($N =$

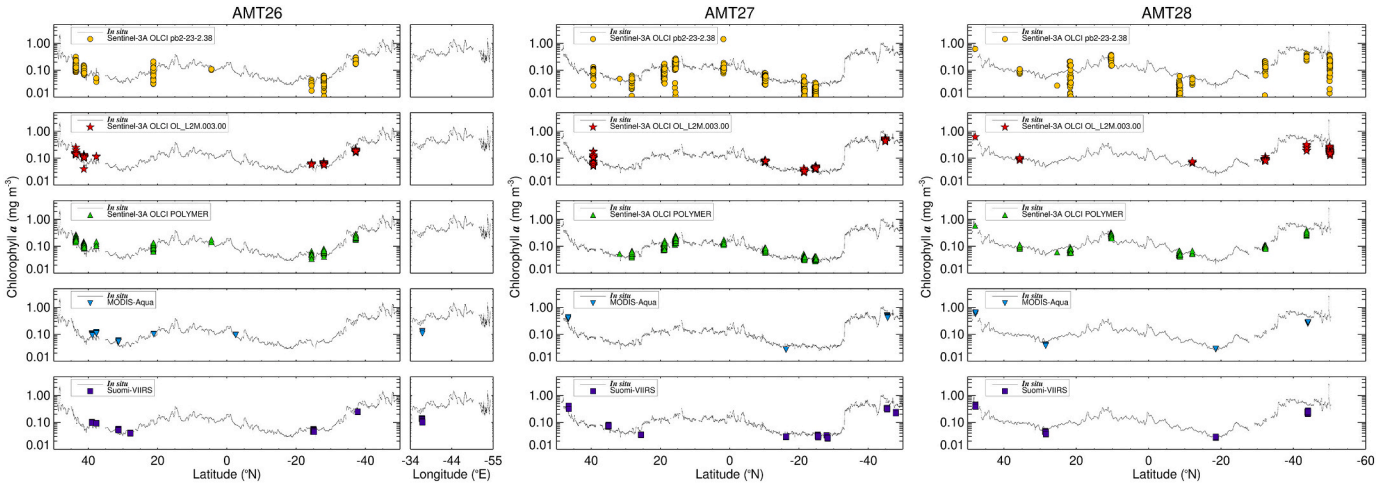

Fig. 5. Variability in *in situ* ACS Chl *a* (grey line), S-3A OLCI Chl *a* pb 2.23–2.29 (yellow circles), S-3A OLCI Chl *a* OL_L2.003.00 (red stars), S-3A OLCI Chl *a* POLYMER v4.8 (green triangles), MODIS-Aqua OCx Chl *a* (light blue inverted triangles) and VIIRS OCx Chl *a* (dark blue squares) on AMT26, 27, 28. (For interpretation of the references to colour in this figure legend, the reader is referred to the web version of this article.)

435), the performance and differences between each AC processor remained similar (Fig. 3d, e, f). S-3A OLCI pb 2.23–2.29 (OC4Me) still exhibited a large offset especially at low Chl *a* with a high scatter around the 1:1 line, which resulted in a high slope, intercept, negative bias, RMSD and RPD of 36% (Fig. 3d). The performance of S-3A OLCI Chl *a* OL_L2M.003.00 (OC4Me + CI) improved and the slope was closer to 1, the intercept, bias and RMSD were smaller and the RPD was reduced to 24% (Fig. 3e). The performance of S-3A OLCI POLYMER also improved as there was less scatter which resulted in a lower intercept and a smaller positive bias, though the RPD was similar (~21%; Fig. 3f).

3.2. Comparison of OLCI Ocean-colour algorithms with MODIS-aqua and VIIRS

Scatter plots of *in situ* Chl *a* against MODIS-Aqua and VIIRS standard Chl *a* algorithms (R2018) are given in Fig. 4 for match-ups common with S-3A OLCI. Due to the difference in over-pass times between MODIS-Aqua, VIIRS and S-3A OLCI, there were fewer match-ups for the NASA sensors (MODIS-Aqua $N = 78$; VIIRS $N = 88$). VIIRS exhibited an over-estimate at low Chl *a* and an under-estimate at higher Chl *a* values and tended to have a high scatter, which resulted in a high intercept, bias, RMSD and RPD of 35%. MODIS-Aqua was more accurate, having a low intercept, bias and RMSD, a slope and percentage variance explained close to 1 and an RPD of 22%. Compared to the NASA products, S-3A OLCI Chl *a* POLYMER still showed the best performance and was slightly more accurate than MODIS-Aqua (Figs. 3, 4). The spatial location of the match-ups for OLCI using the three different Chl *a* algorithms, MODIS-Aqua, Suomi-VIIRS and in relation to *in situ* ACS Chl *a* are given in Fig. 5. S-3A OLCI pb 2.23–2.29 exhibited an under-estimate in Chl *a* at low to medium concentrations. The match-up locations for S-3A OLCI OL_L2M.003.00 were reduced due to the effect of the new flags, but the Chl *a* concentrations were much closer to the *in situ* ACS Chl *a* values. For S-3A OLCI POLYMER v4.8, the number of match-ups were comparatively high and the resulting Chl *a* concentrations were similar to the *in situ* ACS Chl *a* values. For MODIS-Aqua and VIIRS, the number of match-ups were far lower than for S-3A OLCI, but both sensors exhibited realistic Chl *a* concentrations that were similar to the *in situ* ACS Chl *a* values.

3.3. Comparison of sentinel-3A and S-B OLCI tandem phase ocean-colour algorithms

During AMT28, there were 10 coincident images from S-3A and S-3B OLCI with *in situ* ACS Chl *a*, which provided between 164 and 142 match-ups with S-3A, 140 and 121 match-ups with S-3B and 80 coincident S-3A and S-3B match-ups. Both S-3A OLCI Chl *a* pb 2.29 and S-3B OLCI Chl *a* pb 1.30 exhibited an under-estimate of Chl *a* at low values for independent (Fig. 6) and coincident match-ups (Fig. 7), which was greater for S-3A compared to S-3B. For independent match-ups, S-3A pb 2 had a lower I and S closer to 1 compared to S-3B, whereas the Ψ, δ and Δ were lower for S-3B, which resulted in an RPD of 37% for S-3B compared to 39% for S-3A (Fig. 6). For coincident match-ups, S-3B was more accurate for all metrics and within 34% of *in situ* ACS Chl *a* (Fig. 7) and for S-3A, the under-estimate in Chl *a* increased. For OL_L2M.003.00 the range in Chl *a* for S-3B (0.035 to 0.1 mg m^{-3}) was smaller than for S-3A (0.06 to 0.2 mg m^{-3}), which tended to under-estimate Chl *a* at concentrations between 0.1 and 0.2 mg m^{-3}. The δ and Δ for S-3B were consistently lower than those of S-3A Chl *a* OL_L2M.003.00 resulting in an RPD of 21% for S-3A and 11% for S-3B. For coincident match-ups the RPD was ~9% for both OLCI S-3A and S-3B (Fig. 7). Using OLCI POLYMER for both S-3A and S-3B, the points converged to the 1:1 line, which significantly reduced the bias and RMSD resulting in a RPD of 18% and 11% respectively for independent match-ups, and 20% and 11% respectively for coincident data (Figs. 6, 7).

3.4. Accuracy assessment of ocean colour algorithms for OLCI in the Atlantic Ocean using in situ R_{rs} (λ)

To further assess the cause of the differences between the satellite Chl *a* products, the R_{rs} spectra from *in situ* measurements, S-3A OLCI pb 2.23–2.29, OL_L2M.003.00, POLYMER v4.8, MODIS-Aqua and Suomi-VIIRS are compared at the match-up stations (Fig. 8). The differences between *in situ* and satellite R_{rs} are further quantified in Fig. 9. To compute Chl *a*, S-3 OLCI OC4Me utilises R_{rs} at 442, 490, 510 and 560 nm, OC3 for MODIS-Aqua uses R_{rs} at 443, 488 and 555 nm and OC3 for VIIRS uses R_{rs} at 443, 486 and 551 nm. Additionally, the CI algorithms for S-3A OLCI, MODIS-Aqua and VIIRS also deploy 665, 667 and 671 nm respectively, to compute Chl *a* in oligotrophic waters. S-3 OLCI POLYMER utilises all bands from 412 to 560 nm to derive Chl *a* concentrations. There were $N = 140$ coincident R_{rs} spectra between the *in situ* and satellite measurements. Qualitatively, the closest match to *in situ* R_{rs} was

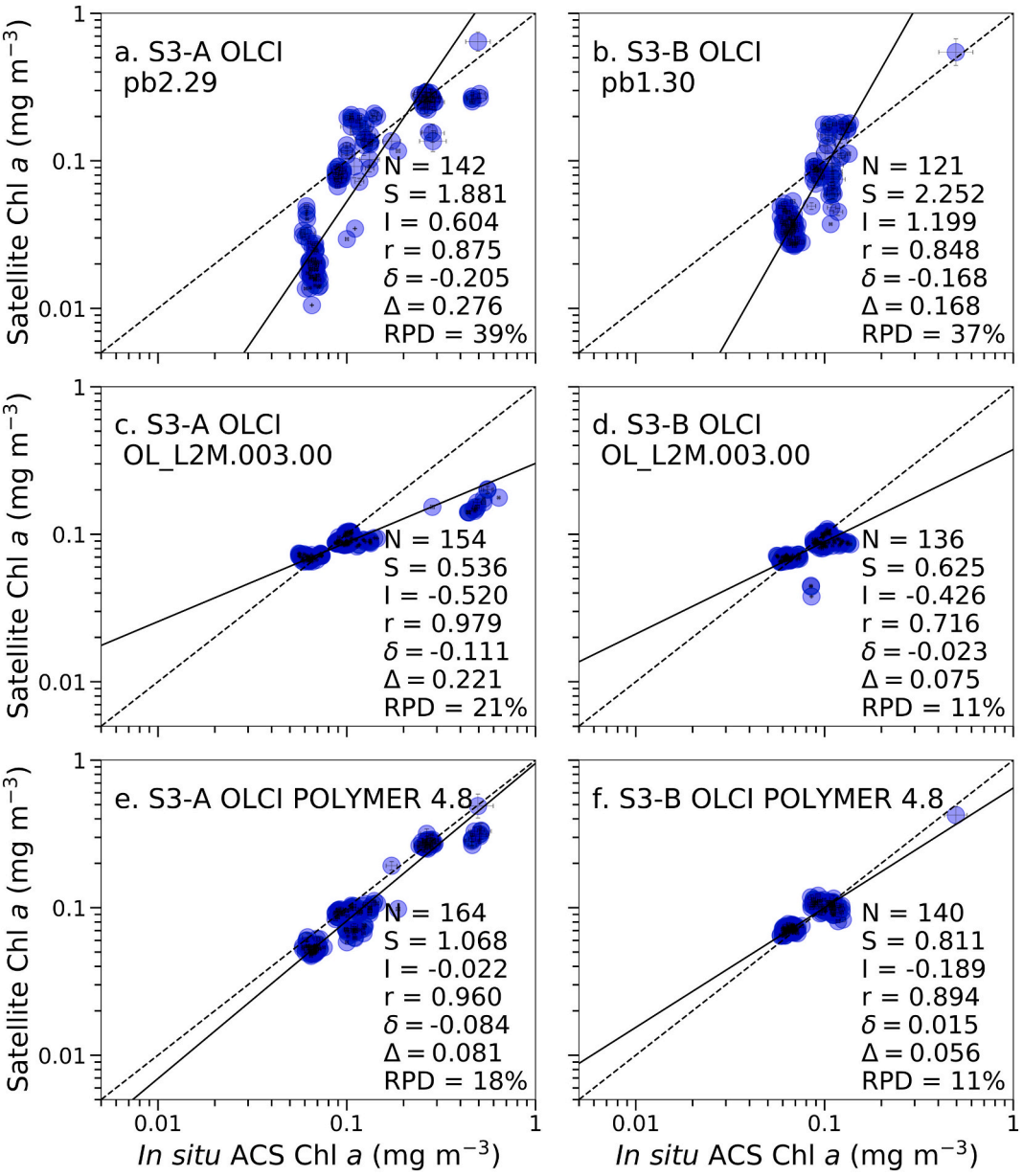

Fig. 6. Scatter plot of *in situ* ACS Chl *a* from AMT28 *versus* (Aa.) S-3A OLCI Chl *a* pb 2.29 (OC4Me), (b.) S-3B OLCI Chl *a* pb 1.30 (OC4Me), (c.) S-3A OLCI Chl *a* OL_L2M.003.00 (OC4Me + CI) (d.) S-3B OLCI Chl *a* OL_L2M.003.00 (OC4Me + CI), (e.) S-3A OLCI Chl *a* POLYMER, (D.) S-3B OLCI Chl *a* POLYMER, for independent match-ups.

S-3A OLCI POLYMER, though the variance in POLYMER R_{rs} at 560 to 665 nm was far less than the *in situ* R_{rs}. The spectral shape of S-3A OLCI pb 2.23–2.29 and OL_L2M.003.00 R_{rs} was higher in the blue and for pb 2.23–2.29 there were systematic differences in the shape of R_{rs} at 490 nm and the variance in blue-green to red bands was always higher. To quantify these patterns, the residuals between *in situ* and satellite R_{rs} showed that for the OLCI AC processors at 443 and 490 nm, POLYMER was more accurate with a mean difference of 6% and 4% respectively, whereas OL_L2M.003.00 had a mean difference of 9% and 9%, respectively. At 560 and 665 nm however, OL_L2M_003.00 performed better with a mean difference of 9% and 12% respectively, compared to 16% and 61% for POLYMER. VIIRS at 443 nm was similar (6% mean difference) to OLCI POLYMER. Both MODIS-Aqua and VIIRS performed better than S-3 A OLCI processors in the green and at 555 and 551 nm, with mean differences of 0.2% and 1%, respectively. The variance in R_{rs} spectra for S-3A OLCI pb 2 at 510 and 560 nm and for MODIS-Aqua at 412 nm was high (Fig. 8), and the residual differences with *in situ* R_{rs} were > 100% (Fig. 9). Similarly at red bands, the residual differences of some outliers for all AC processors were > 300% and for the OLCI processors and MODIS-Aqua at 667 and 678 nm these were > 400% (Fig. 9).

To further assess the performance of OC4Me, *in situ* R_{rs} measured during the three AMT field campaigns was used to estimate Chl *a* and the associated variance in both the ACS Chl *a* and HyperSAS R_{rs} data were computed based on the standard deviation in $\log_{10}$ space of each coincident data point (Fig. 10). Compared to the OLCI pb 2.23–2.29, the performance of OC4Me was improved using *in situ* R_{rs}, with the slope and percentage variance explained closer to 1 and a lower intercept and bias. There was however, a small under-estimate in Chl *a* compared to the *in situ* ACS Chl *a*, implying that the OC4Me may require retuning for the Atlantic Ocean. Including the standard deviation in both the *in situ* ACS Chl *a* data and R_{rs}, the regression line still falls outside of the bounds of the spatial variability, suggesting a systematic bias in OC4Me which amounts to 25%. There are three points at higher Chl *a* concentrations

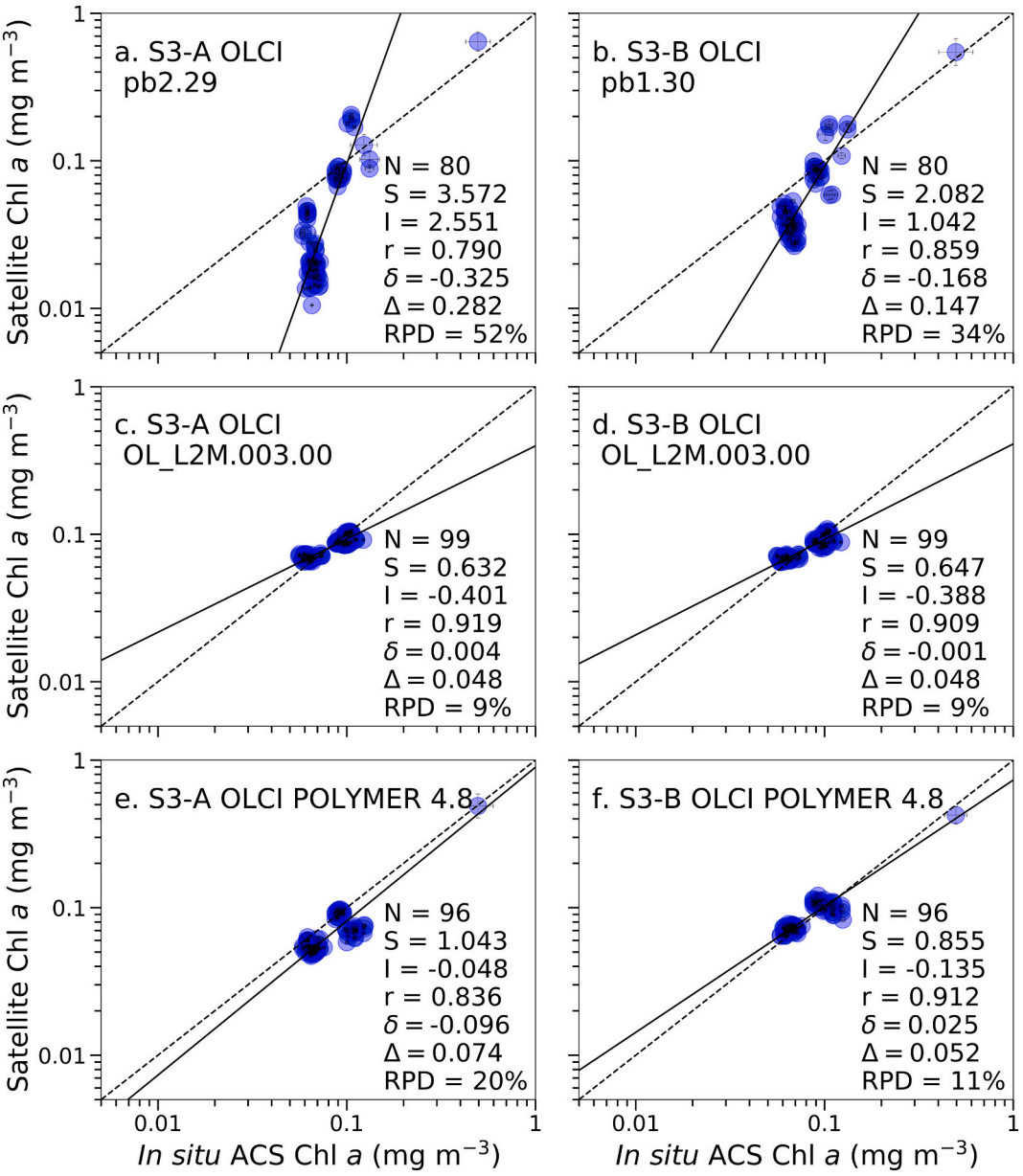

Fig. 7. Scatter plot of *in situ* ACS Chl *a* from AMT28 *versus* (Aa.) S-3A OLCI Chl *a* pb 2.29 (OC4Me), (b.) S-3B OLCI Chl *a* pb 1.30 (OC4Me), (c.) S-3A OLCI Chl *a* OL_L2M.003.00 (OC4Me + CI), (d.) S-3B OLCI Chl *a* OL_L2M.003.00 (OC4Me + CI), (e.) S-3A OLCI Chl *a* POLYMER, (D.) S-3B OLCI Chl *a* POLYMER, for coincident match-ups.

where the uncertainty is particularly large (Fig. 10).

3.5. Spatial comparison between ocean-colour satellite sensors and algorithms over the oligotrophic Atlantic Ocean gyres

During the three AMT campaigns, the Chl *a* concentration varied between 0.04 and 0.1 mg m^{-3} in the northern gyre and between 0.02 and 0.1 mg m^{-3} in the southern gyre, with the lowest concentration recorded in both gyres during AMT27 (Fig. 2). Composite ocean-colour satellite images from S-3A OLCI using the three Chl *a* algorithms, as well as from MODIS-Aqua and VIIRS for the north (12th – 19th October 2018) and south Atlantic gyres (10th – 17th October 2017) are given in Fig. 11. For both the north and south Atlantic gyres, S-3A OLCI POLYMER consistently gave the highest Chl *a* concentrations. In the centre of both the north (25–30°N, 40–70°W) and south (20–25°S, 10–40°W) gyres, which was ~0.06 mg m^{-3} (Fig. 11). By comparison, Chl *a* concentrations from OLCI pb 2.23–2.29 in the centre of the north and south gyres were far lower (0.01–0.03 mg m^{-3}), MODIS-Aqua and VIIRS returned values between 0.02 and 0.04 mg m^{-3}, whereas OLCI OL_L2M.003.00 gave values of 0.03–0.05 mg m^{-3}. For the coverage, especially in south Atlantic gyre, S-3A OLCI POLYMER Chl *a* had the highest coverage and S-3A OLCI pb 2.23–2.29 the lowest with some of the area north of 20.0°S and between 25 and 15°W affected by cloud cover.

To further assess the differences between the ocean colour Chl *a* in both space and time, daily data were extracted from the north (35–20°N; 30–75°W) and south Atlantic (30–15°S; 05–35°W) gyres over the S-3A OLCI time series during the field campaigns in 2016, 2017, 2018. Daily average Chl *a* concentration, number of valid pixels and % coverage were compared between OLCI (for the three AC algorithms), MODIS-Aqua and VIIRS products (Figs. 12, 13). Among the missions, there are differences in pixel sizes and swath-widths. The patterns in the data were similar between products for both the north and south Atlantic gyre but the magnitude of the values differed. Over both the north and

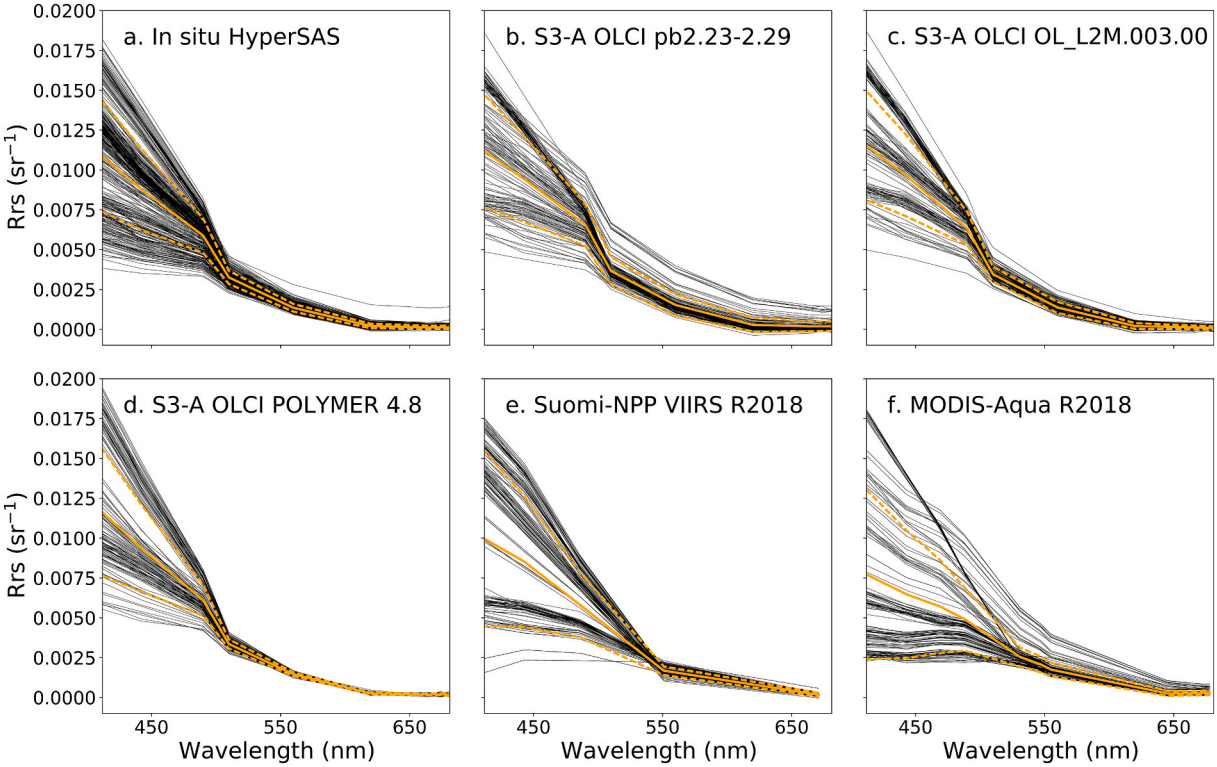

Fig. 8. Comparison of R_{rs} spectra from *in situ* HyperSAS, S-3A OLCI pb 2.23–2.29, S-3A OLCI OL_L2M.003.00, S-3A OLCI POLYMER v4.8, MODIS-Aqua R2018, VIIRS R2018 in the Atlantic Ocean. The black lines are R_{rs} spectra coincident with the *in situ* data, the solid orange line is the mean, the dashed orange lines are ±1 standard deviation. (For interpretation of the references to colour in this figure legend, the reader is referred to the web version of this article.)

south Atlantic gyres, OLCI POLYMER consistently returned the highest Chl *a* values, the highest number of valid pixels and therefore, the highest % coverage (Figs. 12, 13). In the north and south gyre, S-3A OLCI pb 2.23–2.29 consistently returned the lowest Chl *a* concentrations and both this algorithm and S-3A OLCI OL_L2M.003.00 had the lowest number of valid pixels and the lowest % coverage, consistent with the smaller swath-width. MODIS-Aqua and VIIRS Chl *a* concentrations and number of valid pixels were greater than S-3A OLCI pb 2.23–2.29, but less than S-3A OLCI POLYMER. The higher number of pixels available for MODIS-Aqua and VIIRS is in part due to the higher swath-width for these sensors.

For S-3A OLCI POLYMER the range in Chl *a* was 0.05 to 0.09 mg m^{-3} in the north Atlantic gyre from 12th to 19th October 2018 (Fig. 11a). In the south Atlantic gyre, Chl *a* varied from 0.06 to 0.1 mg m^{-3} during 10th to 17th October 2017 (Fig. 11b). By comparison, for S-3A OLCI pb 2.23–2.29 the range in Chl *a* values was 0.03 to 0.06 mg m^{-3} in the north gyre and 0.03 to 0.08 mg m^{-3} in the south gyre. For each campaign in the north gyre, an equator-ward increase in Chl *a* (Fig. 11a) was associated with a reduction in the number of valid pixels, which caused a slight decrease in the % coverage (Fig. 12). In the south gyre, there was a similar equator-ward increase in Chl *a* concentration (Fig. 11b), but there was no clear association or inverse trend in valid pixels and % coverage (Fig. 13). During 2016, the number of valid pixels in the south gyre increased slightly during the campaign, in 2017 they stayed the same and in 2018 they decreased over time (Fig. 13).

4. Discussion

4.1. Using underway measurement systems to maximise satellite match-ups and capture the variability in ocean and atmosphere conditions

Historically, *in situ* R_{rs} and Chl *a* data were obtained from on station deployments of profiling radiometers and coincident Chl *a* concentrations from water bottle samples, which resulted in few match-ups with satellite data. The first version of SeaBASS for example, was comprised of seven years of *in situ* data (1989–1996) with a total of 442 HPLC Chl *a* data. These included two AMT campaigns (AMT1 and 2) with a total of 33 HPLC Chl *a* data (O'Reilly et al., 1998). Once these data are filtered for match-ups within ±1.5 h of the satellite overpass, and satellite observations are masked through standard data quality flags, the number of data is closer to only 6 per AMT cruise. For the three AMT field campaigns in this study, there would have been a maximum of 17 match-ups based on discrete HPLC Chl *a* data. Of the validation studies of S-3 OLCI Chl *a* products published to date, those that have used discrete HPLC, spectrophotometric and fluorometric Chl *a* measurements resulted in $N = 20$, 60 and < 100 match-ups (Liu et al., 2021, Kratzer and Plowey, 2021, Giannini et al., 2021), respectively. By comparison, the only study to date that deployed an underway *in situ* ACS Chl *a* system to validate S-3 OLCI, resulted in $N = 3000$ match-ups (Liu et al., 2018). In this study, the deployment of underway spectrophotometers on AMT26, 27 and 28 provided 96,374 highly accurate (~8% uncertainty) Chl *a* data with 742 match-ups from 17 satellite images for OLCI OL_L2M.003.00, with each match-up having an independent set of *in situ* data. This is approximately 250 match-ups per AMT campaign and is a significant advancement in developing semi-autonomous instruments for the validation of ocean-colour Chl *a* products at high resolution in remote locations of the global ocean. For autonomous measurements, the number of match-ups can be increased at high spatial and temporal frequencies. Using these methods, there will however be a certain level of auto-correlation in time and space between adjacent pixels, especially in regions with very stable in water conditions such as the oligotrophic ocean gyres. However, the variability in the ocean is not the only factor to consider when validating ocean colour satellite algorithms. The spatio-temporal variability of the atmosphere, which affects the atmospheric correction of satellite data, also needs to be considered. Crucially, the atmosphere is characterised by much

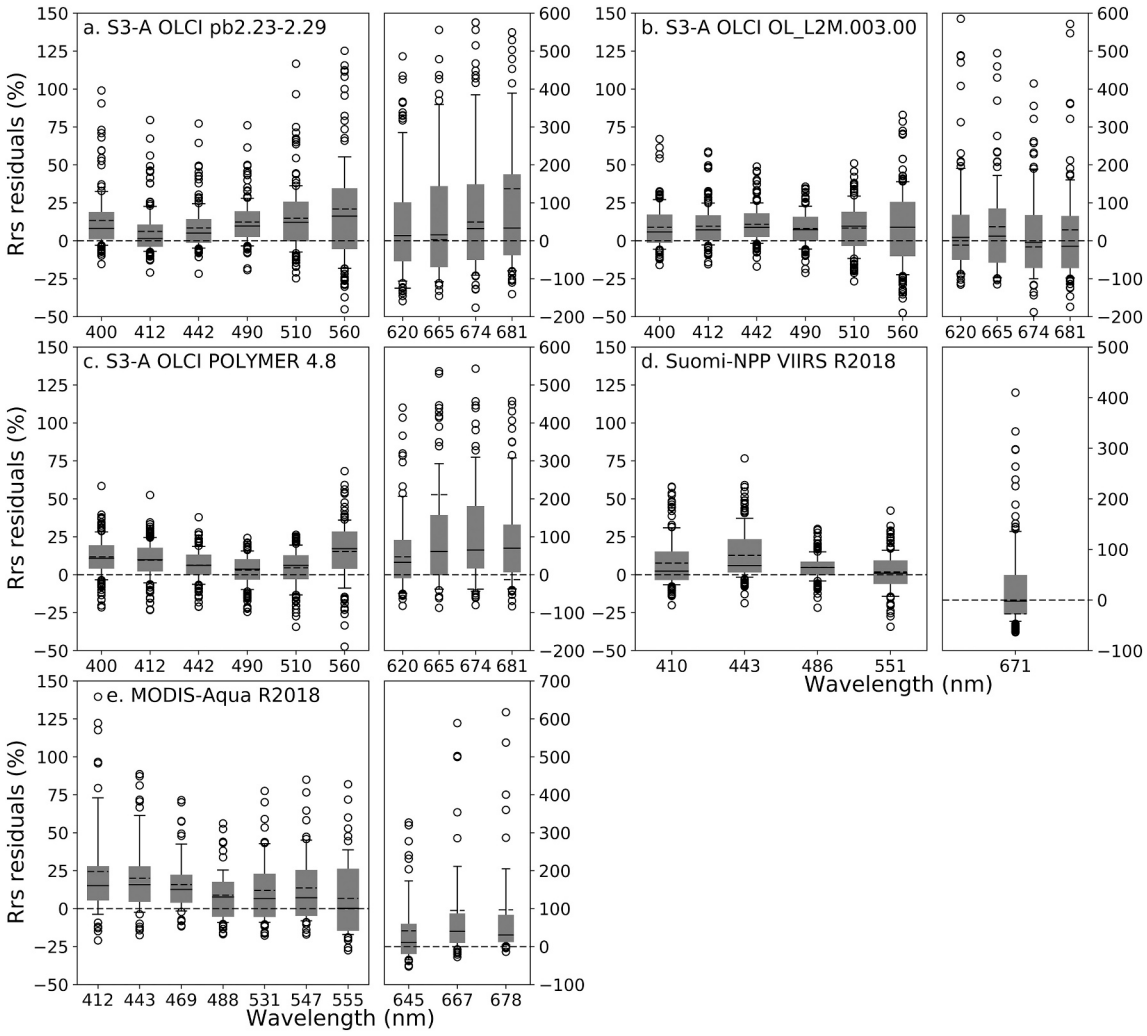

Fig. 9. Residuals of R_{rs} for each satellite algorithm expressed as a percentage difference to the *in situ* R_{rs} at each wavelength. The residuals for each satellite algorithm are calculated as [(*satellite* R_{rs} – *in situ* R_{rs}) / *in situ* R_{rs}]*100. The *in situ* R_{rs} is given as the horizontal dotted line. For the box plot, the lower boundary of the box is the 25th percentile, the solid line within the box is the median, the dashed line is the mean and the upper boundary of the box is the 75th percentile. The error bars above and below the box indicate the 90th and 10th percentiles respectively, and the points beyond the error bars are outliers.

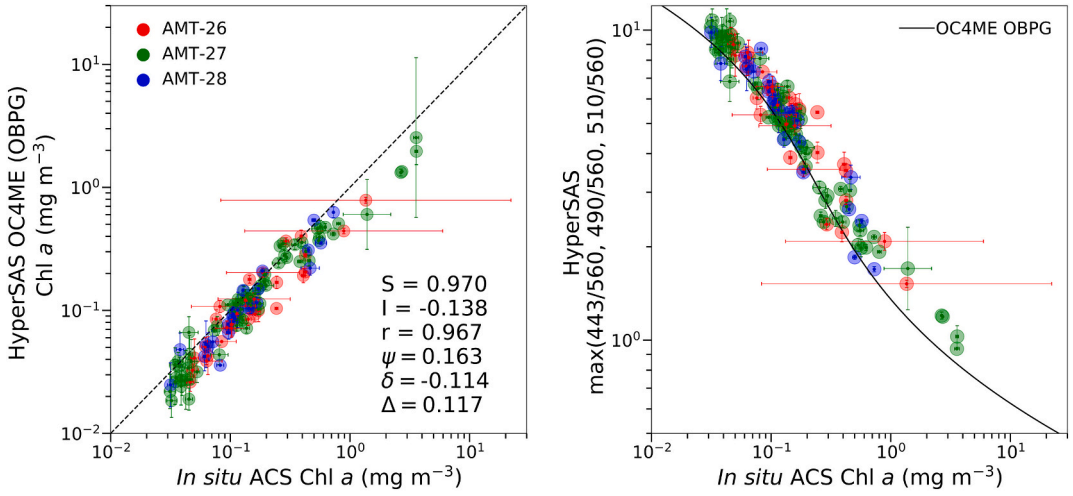

Fig. 10. Scatter plot of *in situ* ACS Chl *a* from AMT26, 27 and 28 *versus* OC4Me run using *in situ* R_{rs}, and the value of the maximum band ratio calculated from *in situ* R_{rs}. The error bars are the standard deviation in *in situ* ACS Chl *a* and R_{rs} HyperSAS measurements calculated for each station using $\log_{10}$ transformed data extracted over the 1 h period of the sampling duration.

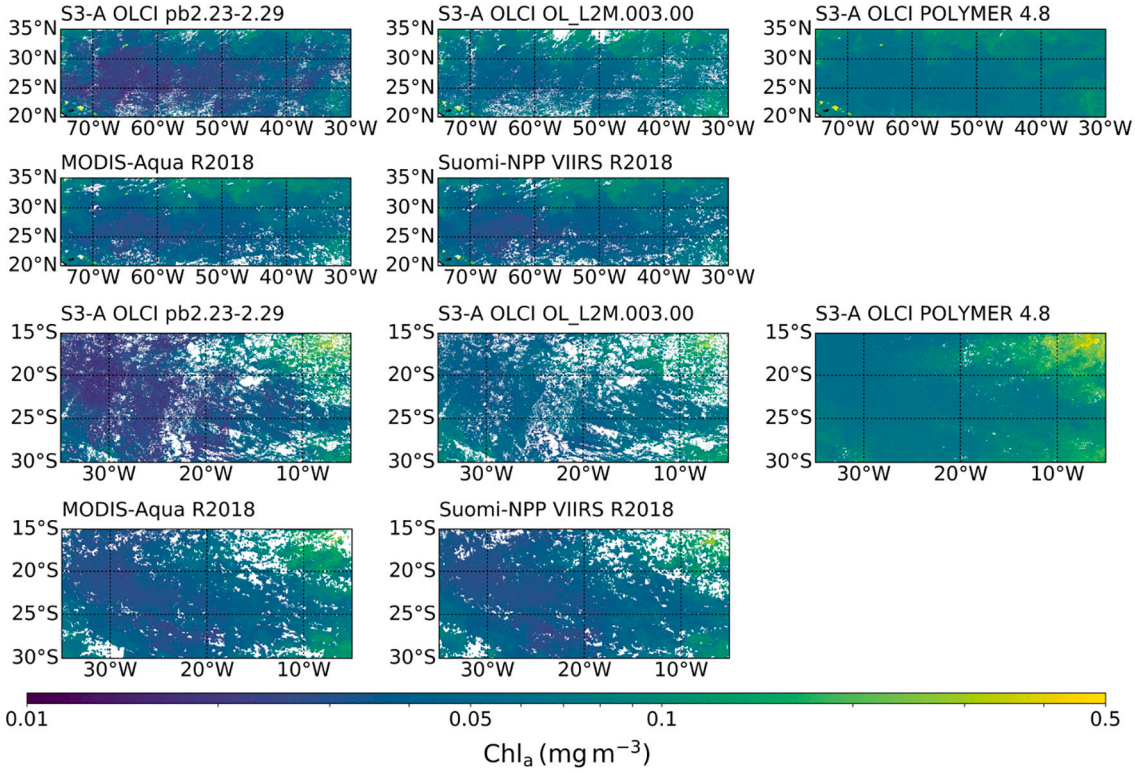

Fig. 11. Comparison of composite satellite images of S-3A OLCI pb2.23–2.29 Chl *a* (OCMe), S-3A OLCI POLYMER Chl *a*, S-3A OLCI OL_L2M.003.00 Chl *a* (OCMe+CI), MODIS-Aqua Chl *a*, Suomi-NPP VIIRS Chl *a* for (a.) north Atlantic Gyre from 12th – 19th October 2018 and (b.) south Atlantic Gyre from 10th – 17th October 2017. (For interpretation of the references to colour in this figure legend, the reader is referred to the web version of this article.)

shorter de-correlation scales than the ocean (*i.e.*, hours *versus* days to weeks). Thus, even under relatively stable oceanic regions, high-resolution *in situ* measurements are also required to assess variability in the atmospheric correction processor. This is illustrated by comparing *in situ* and satellite Chl *a* in the oligotrophic waters of the Atlantic ocean at concentrations <0.1 mg m^{-3} (Fig. 3a). While there is little variability in the *in situ* Chl *a* values, the variability in the retrieved satellite S-3A OLCI pb 2.23–2.29 Chl *a* can be large and is not correlated with the *in situ* data. The higher variability in the satellite retrievals suggests that the atmospheric correction should be improved. If we had obtained only one match-up point per image, we would not have been able to identify this variability and error in S-3A OLCI pb 2.23–2.29. Perhaps part of the reason why S-3A OLCI POLYMER performs better than pb 2.23–2.29 (Fig. 3a, c), is that the POLYMER atmospheric model reproduces well the scattering by the atmosphere under these conditions (Steinmetz et al., 2011), whereas the AC for pb 2 does not reproduce the variability in the atmospheric conditions accurately. Some studies have assessed the temporal and spatial variability of the ocean (Stock and Subramaniam, 2020; Glover et al., 2018). More work is required to quantify the extent to which *in situ* measurements also represent the atmospheric variability over specific ocean regions (Zibordi et al., 2015).

4.2. Performance of OLCI AC processors in determining Chlorophyll-a

To meet the goals of the NASA mission, the aspiration for SeaWiFS was that satellite derived R_{rs} should be ±5% of *in situ* reference measurements (McClain et al., 2004). If this is met, the accuracy of Chl *a* retrieved from satellite R_{rs} is expected to be <35% (Bailey and Werdell, 2006). The OC4 Chl *a* algorithms and associated band ratio variants have been operationally used for the past two decades and have proven to be robust in the open-ocean (O'Reilly et al., 1998). S-3 OLCI's Chl *a* algorithm level 2 processing chains have been evolving. For pb 2 only OC4Me is implemented. From 2021 onwards, the updated OL_L2M.003.00 processor implements both CI and OC4Me for S-3A and S-3B. The CI algorithm is applicable in oligotrophic waters at Chl *a* concentrations ≤0.25 mg m^{-3} (Hu et al., 2012), which represent 78% of the global ocean area. NASA implemented the CI algorithm in its 2014.0 reprocessing, which significantly improved the quality and consistency of images between SeaWiFS, MODIS-Aqua and VIIRS in oligotrophic oceans (Hu et al., 2019). The CI is also reported to be more tolerant to errors in the AC, which potentially reduces artefacts in the resulting imagery (Brewin et al., 2015b; Hu et al., 2019; Wang and Son, 2016). The CI is however, also empirical by design and therefore may exhibit the same uncertainties due to variability in the inherent optical properties (IOPs), absorption coefficient of coloured dissolved material (a_{CDOM}), absorption coefficient of detrital material (a_{DM}) across different ocean basins and regions (Szeto et al., 2011).

The first objective of this paper was to determine which Chl *a* algorithm(s) for S-3 OLCI perform best. The second objective was to evaluate which Chl *a* algorithm(s) for OLCI S-3A and S-3B perform best. Evaluation of which OLCI algorithm(s) perform best is important, as OLCI will become the primary ocean colour observing satellite over the next decade and it's accuracy needs to be monitored over the life time of the mission. The observation capability of S-3 OLCI is enhanced by using a constellation of three sensors; S-3A, S-3B and S-3C each with a 7 year lifespan. Each pair of OLCI sensors will be flown in tandem for a brief period, which enables comparison OLCI sensor specific products (Donlon et al., 2012). This is the first paper that compares S-3A and S-3B Chl *a* products in the tandem phase of the missions. For S-3A OLCI alone using a larger number of match-ups taken from three AMT field campaigns, POLYMER performed best. For OLCI S-3A and S-3B using *in situ* ACS Chl *a* from one AMT field campaign, S-3B performed better than S-3A with OLCI pb 2 and POLYMER, whereas for OL_L2M.003.00 the performance of S-3B and S-3A were similar. The reasons for this are discussed in the following section.

The accuracy of ocean-colour Chl *a* depends on the spectral shape of

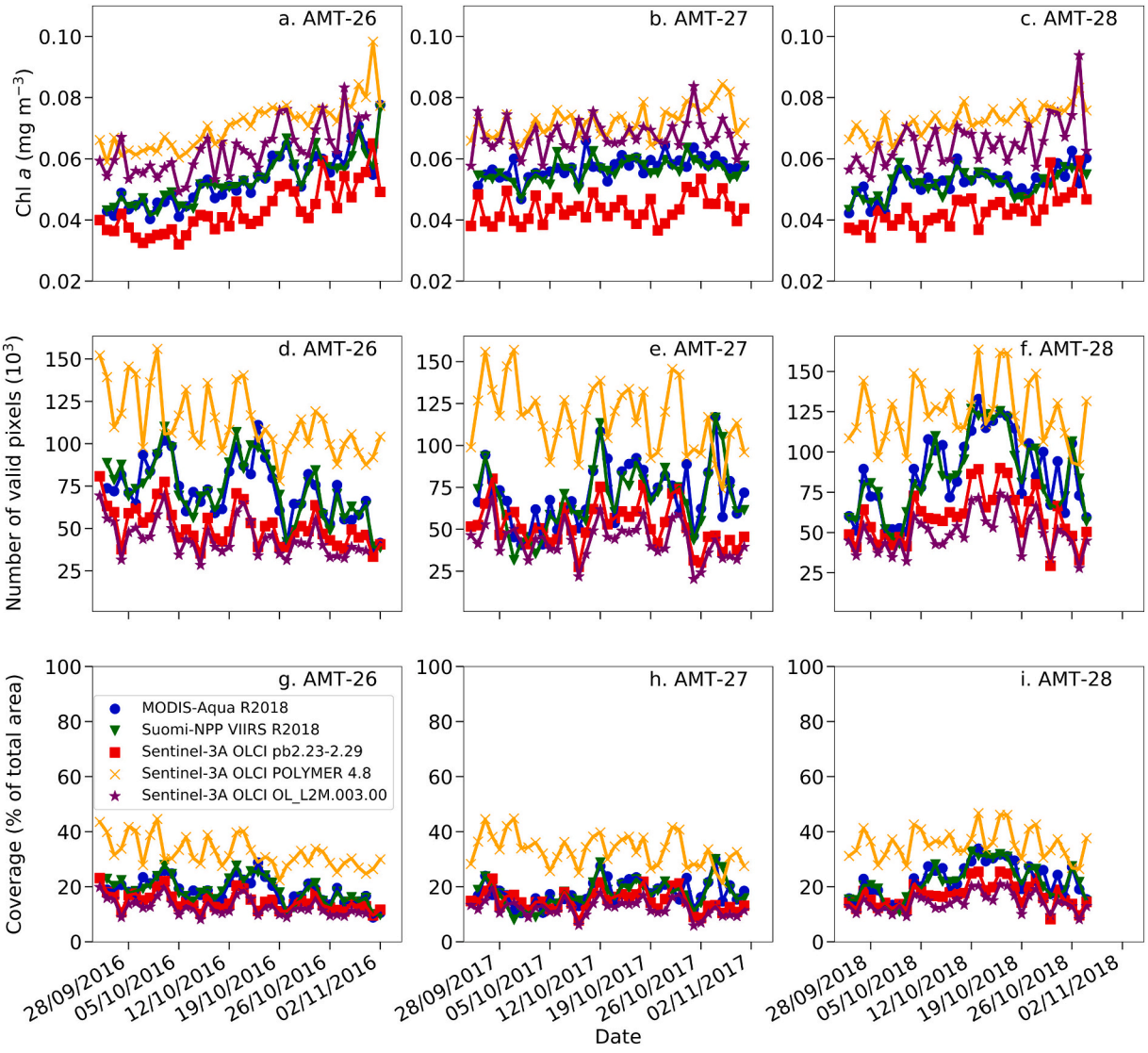

Fig. 12. Average Chl *a* concentration from each satellite algorithm (S-3A OLCI pb 2.23–2.29, pb OL_L2M.003.00, POLYMER, NASA MODIS-Aqua and Suomi-NPP VIIRS) over the North Atlantic Gyre during (a.) AMT26, (b.) AMT27, (c.) AMT28. The number of valid pixels for each sensor is given in (d.) AMT26, (e.) AMT27, (f.) AMT28 and the percentage of the coverage area is given in (g.) AMT26, (h.) AMT27, (i.) AMT28. (For interpretation of the references to colour in this figure legend, the reader is referred to the web version of this article.)

R_{rs}, which can be affected by atmospheric artefacts and water surface conditions such as glint and whitecaps, other water constituents, and by the uncertainties in the satellite derived L_{TOA} signal. If the AC can be improved, the error in satellite R_{rs} and Chl *a* can be reduced and the signal from particles in seawater to $L_{TOA}(\lambda)$ can be more accurately quantified. After more than 2 decades of operational ocean-colour products, the AC still remains one of the most challenging problems to improving satellite ocean-colour data. To assess where the errors in Chl *a* from the algorithms may arise, coincident spectra for *in situ* R_{rs}, S-3A OLCI, MODIS-Aqua and VIIRS were compared along the AMT campaigns (Figs. 8, 9). Of the S-3 OLCI AC processors tested, the closest match to *in situ* R_{rs} at 442, 490 and 510 nm was POLYMER, which exhibited a 6, 4 and 6% difference, respectively, but had a larger difference (17%) at 560 nm compared to the other processors. Evidently the low error in R_{rs} retrieval by POLYMER led to the best performance in the retrieval of Chl *a* among the OLCI algorithms tested (Figs. 3, 6, 7). S-3A OLCI pb2.23–2.29 R_{rs} were consistently higher at 490, 510 and 560 (10, 12, 16%, respectively) compared to OL_L2M.003.00 (7, 10, 9%; Fig. 9), and some of the pb 2 spectra exhibited artefacts in shape at 490 and 510 nm (Fig. 8). The over-estimate in R_{rs} at these bands by S-3A OLCI pb 2.23–2.29 leads to a higher blue to blue-green band ratio, which in turn leads to the under-estimate in Chl *a* that is apparent in both S-3A (Figs. 3a, d, 6a, 7a) and S-3B (Figs. 6b, 7b). The improvement in OL_L2M.003.00 both for S-3A (Fig. 3b, e,) and S-3B (Figs. 6d, 7d) evidently comes from deploying the CI that uses R_{rs} at 442, 560 and 665 nm, which have a low error (9, 9, 12%, respectively; Fig. 9). The under-estimate in Chl *a* at concentrations between 0.2 and 0.8 mg m^{-3} by S-3A OL_L2M.003.00 (Fig. 3b) were similarly due to an over-estimate in the corresponding R_{rs}. These match-up points occurred during AMT27 and 28 at between 33° and 44°S, which is a very dynamic region both in terms of in water constituents and atmospheric gradients. It covers an area from the lowest Chl *a* waters in the Atlantic Ocean of the south Atlantic gyre and the higher Chl *a* waters of the great calcite belt where blooms of coccolithophorids and other phytoplankton extend from the Patagonian shelf into the off-shore waters. In addition, the associated atmospheric conditions are very variable with partial clouds, high wind speeds (>11 m s^{-1}; that can cause white caps) as well as dust blown from the Patagonian desert, which may lead to errors in the associated satellite AC aerosol retrieval. The high scatter evident around the 1:1 line in Fig. 3a and b could also be due to stray and scattered light from clouds as

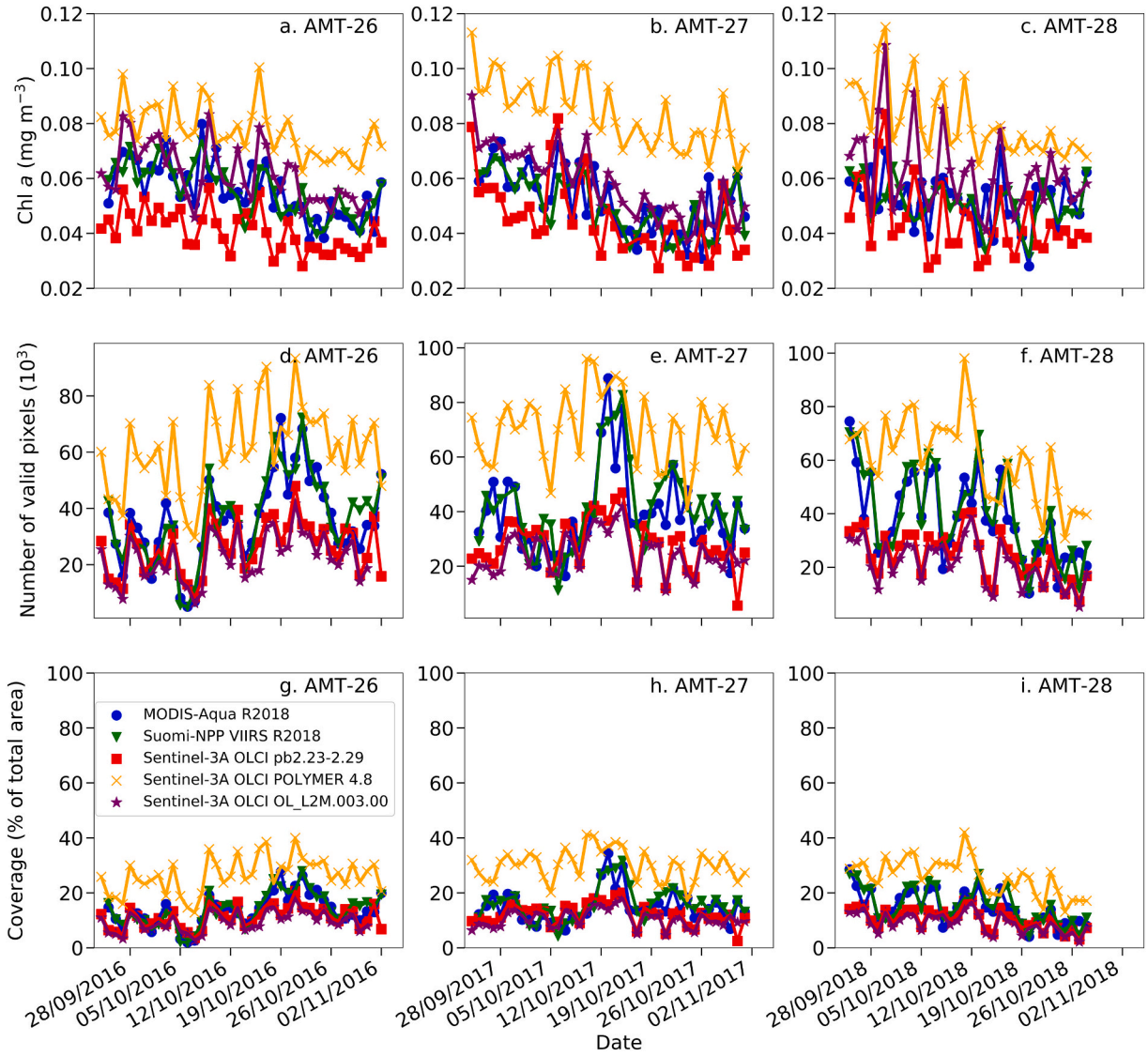

Fig. 13. Average Chl *a* concentration from each satellite algorithm (S-3A OLCI pb 2.23–2.29, pb OL_L2M.003.00, POLYMER, NASA MODIS-Aqua and Suomi-NPP VIIRS) over the South Atlantic Gyre during (a.) AMT26, (b.) AMT27, (c.) AMT28. The number of valid pixels for each sensor is given in (d.) AMT26, (e.) AMT27, (f.) AMT28 and the percentage of the coverage area is given in (g.) AMT26, (h.) AMT27, (i.) AMT28. (For interpretation of the references to colour in this figure legend, the reader is referred to the web version of this article.)

also detected for MODIS-Aqua in previous studies (Meister and McClain, 2010). For the new OL_L2M.003.00 the high scatter at between 0.1 and 1.0 mg m^{-3} Chl *a*, which is the range that corresponds to the implementation of OC4Me or the blending between OC4Me + CI, warrants further investigation. For a smaller number of match-ups, this pattern was less evident in S-3B OLCI Chl *a* compared with S-3A (Fig. 6).

Errors in band-ratio Chl *a* products arise principally from improper AC or non-compliant variability in the IOPs. The relative uncertainties in R_{rs} vary as a function of wavelength and Chl *a* concentration, which either reflect the optical complexity of the water-column or the accuracy of the AC, quality flags and/or cloud masking that is applied. To investigate further the error in S-3A OLCI Chl *a* OC4Me and to remove artefacts arising from improper AC, we used *in situ* R_{rs} to estimate Chl *a* from OC4Me. From this we show that potentially this algorithm underestimates Chl *a* by 25%, because of an over-estimate in the maximum band ratio for Chl *a* (Fig. 10). Even within the bounds of the error bars given in Fig. 10, there is a significant bias in the standard OC4Me in the Atlantic Ocean.

The underlying assumption behind the architecture of the OC4Me band ratio algorithm is that the absorption coefficients of detrital material (a_{DM}) and a_{CDOM} covary with phytoplankton absorption in the open ocean (O'Reilly et al., 1998). At regional scales even in the open-ocean, there can be significant variation in these IOPs depending on the physical, chemical and biological state of the water column. Loisel et al. (2018) and Szeto et al. (2011) showed that OC3 or OC4 can exhibit a a_{DM} bias such that when there is relatively low a_{DM}, OC3 attributes a portion of the reflectance signal to a_{DM} rather than a_{ph} and Chl *a* is underestimated. Similarly, when more a_{DM} is present than expected, OC3 overestimates Chl *a* by assuming some of the a_{DM} signal is due to a_{ph}. In oligotrophic waters when Chl $a < 0.2$ mg m^{-3}, OC3 can underestimate Chl *a* when the algorithm switches to $R_{rs}(443)$ / $R_{rs}(547)$ rather than $R_{rs}(490)$ / $R_{rs}(547)$ (Hu et al., 2012). The differences in the regression slopes between the two band ratios imply that the underlying relationship between the absorption and scattering properties and Chl *a* are different along the gradient in the model. The assumption is that the mean IOP characteristics in these waters are similar to that of the IOP algorithm training set, which may not actually be the case. Dispersion around the mean for band ratios occurs habitually (Brown et al. 2008). Further errors can arise from anomalies in L_{wn} due to either particulate backscattering or from an increase in a_{CDOM} and a_{DM} compared to

phytoplankton, which can cause a systematic bias in satellite Chl *a*. This has been documented for the Mediterranean Sea (Volpe et al., 2007), the Baltic Sea (Pitarch et al., 2016) and the Red Sea (Brewin et al., 2015a). For 11 years of SeaWiFS and MODIS-Aqua, Lee (2010) showed in the South Pacific gyre, that there was a decrease in Chl *a* and a potential increase in a_{CDOM} and a_{DM}, which may increment the error in Chl *a* derived from band ratios. In this study, we do not have a_{DM} data at the same resolution as the Chl *a* data and are unable to investigate further the effect of the IOP's on the resulting Chl *a* concentrations. Further work is required on this, using the semi-autonomous high resolution AMT data sets.

To investigate further the differences between the ocean colour products as mapped images, level 2 Chl *a* products over the north and south Atlantic gyres during October 2018 and 2017 were also compared (Fig. 11). The difference between S-3A OLCI processors was large. For both the north and south Atlantic gyres, S-3A OLCI Chl *a* POLYMER consistently gave higher Chl *a*, had the highest number of valid pixels and the highest % coverage (Figs. 12, 13). POLYMER has been shown to minimise noise whilst increasing the coverage both at global and regional scales (Muller et al., 2015). For the Atlantic Ocean gyres specifically, we also found that for S-3A OLCI Chl *a* POLYMER the coverage is enhanced (Figs. 11, 12, 13). By comparison, S-3A OLCI Chl *a* pb 2.23–2.29 returned a lower number of valid pixels and % coverage over the oligotrophic gyres and the lowest Chl *a* concentrations (Figs. 12, 13). The difference in Chl *a* concentrations between POLYMER and pb 2 from composites arises from differences in flag and cloud masking and the subsequent spatial averaging. Since POLYMER always has a higher coverage compared to pb 2, the average Chl *a* concentrations will always be higher. Thus, the differences that can be seen between the two products in the scatter plots (Fig. 3a, c, d, f) becomes accentuated when averaging over composites and large areas (Figs. 12, 13). The reason for the increased coverage by POLYMER is that the algorithm is accurate when there is sun glint and thin clouds present, since the atmospheric model reproduces well the scattering by the atmosphere under these conditions (Steinmetz et al., 2011; Tan, 2019). The retrieval of Chl *a* by POLYMER utilises a spectral matching of R_{rs} over a range of b_{bNC} and Chl *a* concentrations. If the biogeochemical properties of a region do not fit the training range of the water component of the model or these change over time, then retrieved Chl *a* will be less accurate. As noted by Steinmetz and Ramon (2018), when another free IOP variable, such as a_{CDOM}, is introduced to the POLYMER model, the resulting Chl *a* concentrations can become erroneous (*e.g.* Giannini et al., 2021). Further investigation into the performance of POLYMER with OLCI in other water types, with different IOP constituents and at Chl *a* concentrations >1.0 mg m^{-3}, are necessary before this model can be used with confidence, globally.

4.3. Differences between OLCI, MODIS-aqua and VIIRS Chl a

MODIS-Aqua was launched in 2002, designed to be operational for 6 years and to date is ~18 years old and with MODIS-Terra, is the longest running ocean-colour sensor. In oligotrophic waters, the uncertainty of MODIS-Aqua R_{rs} at blue bands (412–490 nm) when Chl $a \leq 0.1$ mg m^{-3} is 5%, whereas this increases to 5–10% when Chl *a* is between 0.1 and 0.3 mg m^{-3} (Hu et al., 2013). The majority of studies on MODIS-Aqua have shown that the R_{rs} products are accurate, which for green bands are within 20% of *in situ* R_{rs}. These are also in agreement with cross-validation studies between satellite sensors (Barnes and Hu, 2016; Hu et al., 2015; Hu and Le, 2014; Uprety et al., 2013). Historic validation exercises performed at MOBY in the Pacific open-ocean yield a mean absolute relative difference between field and MODIS-Aqua data of approximately 7% between 412 and 490 nm (Mélin et al., 2016). In Mediterranean oligotrophic waters, differences of between 8 and 15% at blue bands have been reported (Zibordi et al., 2011). For MODIS-Aqua in the Ligurian Sea these can be >20% at 412 nm, but within mission requirements at 443 and 490 nm, which yield an uncertainty of ~20% in the Chl *a* product (Antoine et al., 2008). The most comprehensive accuracy assessments of MODIS-Aqua conducted by Mélin and Franz (2014) and Moore et al. (2015) found that the relative uncertainty in R_{rs} is close to the mission target of 5% for blue and blue-green bands in case 1 waters, but exceeds 50% in oligotrophic waters. Recent papers have shown degradation in MODIS-Aqua R_{rs} (Meister and Franz, 2014; Meister et al., 2012), which has been compensated for in the recent R2018 re-processing. Kahru et al. (2015) compared standard ocean colour Chl *a* products for MODIS-Aqua and Suomi-VIIRS over the range from 0.1 to 10 mg m^{-3} and reported an under-estimate in Chl *a* by 9% in the California Current compared to *in situ* Chl *a*. Hu and Le (2014) compared time series measurements of *in situ* Chl *a* with MODIS-Aqua and Suomi-VIIRS NASA data records over Tampa Bay, USA, and reported <25% difference with a mean annual bias of −9% over a Chl *a* range of 1 to 20 mg m^{-3}. At the LISCO AERONET-OC site off Long Island the differences were larger with −26% for Suomi-VIIRS and a 20% difference with MODIS-Aqua (Hlaing et al., 2013).

Very few studies have been conducted comparing S-3 OLCI, MODIS-Aqua and VIIRS, especially in the open-ocean. Li et al. (2019) compared S-3A OLCI, MODIS-Aqua, and Suomi-VIIRS R_{rs} products against *in situ* measurements in the China Sea. All three sensors overestimated R_{rs} in the open ocean and underestimated R_{rs} in coastal waters with the highest uncertainty at the NIR bands. OLCI exhibited an 18% difference at 490 nm and MODIS-Aqua had a 19% difference at 531 nm. Differences in R_{rs} at other bands were higher. Comparing coincident MODIS-Aqua and VIIRS with S-3A OLCI products against the AMT measurements, MODIS-Aqua performed best in the green (0.2% at 555 nm) but had the highest error of all sensors at 443 nm with a difference relative to *in situ* R_{rs} of 16% (Fig. 9). VIIRS R_{rs} performed similarly to S-3A OLCI pb 2.23–2.29 and S-3A POLYMER at 412 and 443 nm, whereas VIIRS R_{rs} in the green performed better than S-3A OLCI with a difference of 1% at 551 nm (Figs. 8, 9). For Chl *a*, S-3A OLCI POLYMER was the most accurate (21%), followed closely by MODIS-Aqua (22%), then S-3A OLCI OL_L2M.003.00 (24%), Suomi-VIIRS (35%) and lastly S-3A OLCI pb 2.23–2.29 (36%). These differences arise because even though the mean VIIRS R_{rs} at blue and green bands appear accurate, there are a large number of the VIIRS spectra that over-estimate R_{rs} (Fig. 8), which causes the under-estimate in Chl *a* at values >0.1 mg m^{-3} (Fig. 4b). Similarly the under-estimate of some VIIRS R_{rs} spectra leads to the over-estimate in Chl *a* at low values when the algorithm switches to the CI (Figs. 8, 4b). The number of match-ups available for MODIS-Aqua and VIIRS coincident with the different S-3A OLCI Chl *a* algorithms was significantly lower due to differences in the spatial resolution (one MODIS pixel is equivalent to 3 × 3 OLCI full resolution pixels), overpass times and the flags applied, which leads the different N shown in Figs. 3, 4, 5. Using S-3A OLCI full resolution data results in far more match-ups than available using the MODIS-Aqua and VIIRS data. The information from the sensors is similar, but the advantage of using S-3A OLCI is that more of the small scale variability on a per pixel basis is captured in these match-ups. Another factor contributing to the reduced number of match-ups for MODIS-Aqua is the stray light flag, which is raised over 3 pixels in the cross-track direction from a cloud pixel and 2 pixels in the along-track direction (Meister and Franz, 2014). The flag is effective in reducing the error from stray light but may be too conservative, leading in part to a reduction in the number of match-ups available. When averaging data over larger spatial areas however, this has a minimal effect on spatial coverage, which for MODIS-Aqua and VIIRS was always higher than S-3A OLCI pb 2 and OL_L2M.003.00 (Figs. 12, 13).

From the results presented, a number of recommendations for further and future development of S-3 OLCI products are identified:

- Underway spectrophotometric semi-autonomous systems deployed on research vessels offer the potential to significantly increase the number of satellite matchup data especially in remote locations of the global ocean, as well as to characterise the spatial variability within satellite pixels. The next step in the development of these

autonomous systems is to characterise the instruments and to construct uncertainty budgets for these data in line with Fiducial Reference Measurements (ISO, 2008).

- Using high resolution *in situ* data available from semi-autonomous systems, further work is required to investigate the de-correlation lengths of oceanic and atmospheric conditions with a view to developing match-up criteria that consider the temporal and spatial variability of these two factors over a site or region.
- The performance of the new OL_L2M.003.00 for S-3A and S-3B OLCI significantly improves the retrieval of Chl *a* in open Atlantic waters, especially at concentrations <0.1 mg m^{-3}, as a result of implementing the CI algorithm. Further investigation into improving the Chl *a* product between the range of 0.1 and 1.0 mg m^{-3} is required.
- The spectral shape of the S-3A OL_L2M.003.00 R_{rs} products is greatly improved compared to pb 2.23–2.29. A slight over-estimate in S-3A OL_L2M.003.00 R_{rs} corresponding to Chl *a* values from 0.1 to 1.0 mg m^{-3} causes an under-estimate in Chl *a* due to potential errors in OC4Me. Understanding the reasons for this (either failure in the AC, associated quality flags and/or the Chl *a* algorithm) will ultimately facilitate future improvement of these products.
- The POLYMER model applied to S-3 OLCI shows great promise in providing accurate Chl *a* concentrations (between 0.01 and 1 mg m^{-3}) and spatially contiguous data, especially in regions where partial cloud and sun glint may affect the retrieval of Chl *a*. Further investigation into the accuracy of S-3 OLCI POLYMER Chl *a* at concentrations >1 mg m^{-3} is required.
- Integration of S-3 OLCI data over the next decade into the existing ocean-colour record will enable discrimination of climate change effects on the marine ecosystem. Utilisation of the POLYMER AC for ocean colour time series will be beneficial for filling gaps in data, both spatially and temporally. Further investigation into the accuracy of ocean colour merged products using the POLYMER AC would be beneficial for both the OC time series and climate change studies for the global ocean.

5. Conclusions

In this paper, we quantify the statistical performance of S-3A OLCI, MODIS-Aqua and Suomi-VIIRS Chl *a* products against *in situ* Chl *a* estimated spectrophotometrically using a quasi-autonomous underway sampling system deployed on three Atlantic Meridional Transect campaigns in 2016, 2017 and 2018. The measurement method for Chl *a* provided ~100,000 measurements over the three campaigns, which resulted in >750 match-ups for S-3A OLCI. This represents a significant advancement in data obtained from remote oligotrophic regions. Using these data, the S-3A and S-3B OLCI pb 2 OC4Me Chl *a* product was compared with OLCI pb 3 and POLYMER as well as standard MODIS-Aqua and VIIRS Chl *a* products. The S-3A OLCI pb 2.23–2.29 Chl *a* exhibited a difference > 35% compared to the *in situ* Chl *a* data. For Suomi-VIIRS, Chl *a* was just within the expected accuracy (~35%) and MODIS-Aqua Chl *a* was within this with a 22% difference compared to the *in situ* ACS Chl *a* data. Of the S-3 OLCI Chl *a* products tested, POLYMER showed the best performance, which was within 20% of *in situ* Chl *a* data. OLCI OL_L2M.003.00 was within 26% of the *in situ* Chl *a*. Both S-3A and S-3B OLCI pb 2.29 and 1.30 Chl *a* exhibited a systematic bias with a consistent underestimate at low Chl *a* values, though S-3B was slightly more accurate than S-3A. There was no such bias in OLCI OL_L2M.003.00 and the accuracy of both S-3A and S-3B OLCI Chl *a* products was imrpoved and exhibited a similar performance. Analysis of coincident images for the five products (3 x OLCI, MODIS-Aqua and Suomi-VIIRS) showed that S-3A OLCI POLYMER had both the highest Chl *a* concentrations and highest % coverage over the north and south Atlantic gyres. S-3A OLCI pb 2.23–2.29 OC4Me produced the lowest Chl *a* and the lowest % coverage. POLYMER is known to provide increased coverage over the global ocean as its polynomial AC model corrects for spectrally homogenous sun glint and thin cloud signatures, while standard AC models often mask the stronger glint and cloud signatures. Based on these results, POLYMER and OL_L2M.003.00 for S-3A and S-3B OLCI show great promise in providing accurate Chl *a* products for these oligotrophic Atlantic waters. Further investigation into the use of POLYMER and OL_L2M.003.00 in other water types, especially with Chl *a* concentrations >1.0 mg m^{-3}, is required. Improvement in S-3 OL_L2M.003.00 Chl *a* in the range from 0.1 to 1.0 mg m^{-3} would also be beneficial.

Declaration of Competing Interest

The authors declare that they have no known competing financial interests or personal relationships that could have appeared to influence the work reported in this paper.

Acknowledgements

The authors would like to thank the captain and crews of *RRS James Clark Ross* on AMT26 and 28 and on *RRS Discovery* for AMT27. We also thank 2 anonymous referees whose comments significantly improved the manuscript. SP, RB, GDO, GT were supported by the AMT4SentinelFRM (ESRIN/RFQ/3-14457/16/I-BG) and AMT4OceanSatFlux (4000125730/18/NL/FF/gp) contracts from the European Space Agency. FN, RB, GDO and GT were also supported by National Capability funding to Plymouth Marine Laboratory for the Atlantic Meridional Transect from the UK Natural Environment Research Council (NERC). In addition, RB and GDO were supported by the National Centre for Earth Observation (NCEO). We would also like to thank the Natural Environment Research Council Earth Observation Data Acquisition and Analysis Service (NEODAAS) for their role in the acquisition of satellite imagery and use of their Linux cluster for processing the satellite data. This is contribution number 343 of the AMT program.

References

Antoine, D., 2010. OLCI Level 2 Algorithm Theoretical Basis Document Atmospheric corrections over Case 1 waters ("Clear Waters Atmospheric Corrections" or "CWAC"). European Space Agency, Report No. S3-L2-SD-03- C07-LOV-ATBD.

Antoine, D., d'Ortenzio, F., Hooker, S.B., Becu, G., Gentili, B., Tailliez, D., Scott, A.J., 2008. Assessment of uncertainty in the ocean reflectance determined by three satellite ocean color sensors (MERIS, SeaWiFS and MODIS-A) at an offshore site in the Mediterranean Sea (BOUSSOLE project). J. Geophys. Res. Oceans 113. https://doi.org/10.01029/02007JC004472. C07013.

Bailey, S.W., Werdell, P.J., 2006. A multi-sensor approach for the on-orbit validation of ocean color satellite data products. Remote Sens. Environ. 102, 12–23. https://doi.org/10.1016/j.rse.2006.01.015.

Barlow, R.G., Cummings, D.G., Gibb, S.W., 1997. Improved resolution of mono- and divinyl chlorophylls a and b and zeaxanthin and lutein in phytoplankton extracts using reverse phase C-8 HPLC. Marine Ecol. Progress Ser. 161, 303–307 (ISSN:1616-1599).

Barnes, B.B., Hu, C.M., 2016. Dependence of satellite ocean color data products on viewing angles: a comparison between SeaWiFS, MODIS, and VIIRS. Remote Sens. Environ. 175, 120–129. https://doi.org/10.1016/j.rse.2015.12.048.

Barnes, B.B., Cannizzaro, J.P., English, D.C., Hu, C.M., 2019. Validation of VIIRS and MODIS reflectance data in coastal and oceanic waters: an assessment of methods. Remote Sens. Environ. 220, 110–123. https://doi.org/10.1016/j.rse.2018.10.034.

Blondeau-Patissier, D., Gower, J.F.R., Dekker, A.G., Phinn, S.R., Brando, V.E., 2014. A review of ocean color remote sensing methods and statistical techniques for the detection, mapping and analysis of phytoplankton blooms in coastal and open oceans. Prog. Oceanogr. 123, 123–144. https://doi.org/10.1016/j.pocean.2013.12.008.

Boss, E.S., Collier, R., Larson, G., Fennel, K., Pegau, W.S., 2007. Measurements of spectral optical properties and their relation to biogeochemical variables and processes in crater Lake, crater Lake National Park, OR. Hydrobiologia 574, 149–159. https://doi.org/10.1007/s10750-006-2609-3.

Brewin, R.J.W., Raitsos, D.E., Dall'Olmo, G., Zarokanellos, N., Jackson, T., Racault, M.F., Boss, E.S., Sathyendranath, S., Jones, B.H., Hoteit, I., 2015a. Regional Ocean-colour chlorophyll algorithms for the Red Sea. Remote Sens. Environ. 165, 64–85. https://doi.org/10.1016/j.rse.2015.04.024.

Brewin, R.J.W., Sathyendranath, S., Muller, D., Brockrnann, C., Deschamps, P.Y., Devred, E., Doerffer, R., Fomferra, N., Franz, B., Grant, M., Groom, S., Horseman, A., Hu, C., Krasemann, H., Lee, Z., Maritorena, S., Meelin, F., Peters, M., Platt, T., Regner, P., Smyth, T., Steinmetz, F., Swinton, J., Werdell, J., White, G.N., 2015b. The ocean colour climate change initiative: III. A round-robin comparison on in-

water bio-optical algorithms. Remote Sens. Environ. 162, 271–294. https://doi.org/10.1016/j.rse.2013.09.016.
Brewin, R.J.W., Dall'Olmo, G., Pardo, S., van Dongen-Vogels, V., Boss, E.S., 2016. Underway spectrophotometry along the Atlantic Meridional transect reveals high performance in satellite chlorophyll retrievals. Remote Sens. Environ. 183, 82–97. https://doi.org/10.1016/j.rse.2016.05.005.
Brown, C.A., Huot, Y., Werdell, P.J., Gentili, B., Claustre, H., 2008. The origin and global distribution of second order variability in satellite ocean color and its potential applications to algorithm development. Remote Sens. Environ. 112, 4186–4203. https://doi.org/10.1016/j.rse.2008.06.008.
Cazzaniga, I., Kwiatkowska, E., 2018. Sentinel-3 OLCI Chlorophyll Index switch for low-chlorophyll waters Algorithm Theoretical Basis Document. EUMETSAT Report, EUM/RSP/DOC/18/1028360.
Chang, N.-B., Imen, S., Vannah, B., 2015. Remote sensing for monitoring surface water quality status and ecosystem state in relation to the nutrient cycle: a 40-year perspective. Crit. Rev. Environ. Sci. Technol. 45, 101–166. https://doi.org/10.1080/10643389.2013.829981.
Dall'Olmo, G., Boss, E., Behrenfeld, M.J., Westberry, T.K., 2012. Particulate optical scattering coefficients along an Atlantic Meridional transect. Opt. Express 20, 21532–21551. https://doi.org/10.1364/OE.20.021532.
Dall'Olmo, G., Westberry, T.K., Behrenfeld, M.J., Boss, E., Slade, W.H., 2009. Significant contribution of large particles to optical backscattering in the open ocean. Biogeosciences 6, 947–967. https://doi.org/10.5194/bg-6-947-2009.
Donlon, C., Berruti, B., Buongiorno, A., Ferreira, M.H., Femenias, P., Frerick, J., Goryl, P., Klein, U., Laur, H., Mavrocordatos, C., Nieke, J., Rebhan, H., Seitz, B., Stroede, J., Sciarra, R., 2012. The global monitoring for environment and security (GMES) Sentinel-3 mission. Remote Sens. Environ. 120, 37–57. https://doi.org/10.1016/j.rse.2011.07.024.
Drusch, M., Del Bello, U., Carlier, S., Colin, O., Fernandez, V., Gascon, F., Hoersch, B., Isola, C., Laberinti, P., Martimort, P., Meygret, A., Spoto, F., Sy, O., Marchese, F., Bargellini, P., 2012. Sentinel-2: ESA's optical high-resolution mission for GMES operational services. Remote Sens. Environ. 120, 25–36. https://doi.org/10.1016/j.rse.2011.11.026.
Dutkiewicz, S., Hickman, A.E., Jahn, O., Henson, S., Beaulieu, C., Monier, E., 2019. Ocean colour signature of climate change. Nat. Commun. 10 https://doi.org/10.1038/s41467-019-08457-x.
Frouin, R., Schwindling, M., Deschamps, P.-Y., 1996. Spectral reflectance of sea foam in the visible and near-infrared: in situ measurements and remote sensing implications. J. Geophys. Res. Oceans 101 (C6), 14361–14371. https://doi.org/10.1029/96JC00629.
Giannini, F., Hunt, B.P.V., Jacoby, D., Costa, M., 2021. Performance of OLCI sentinel-3A satellite in the Northeast Pacific coastal waters. Remote Sens. Environ. 256, 112317. https://doi.org/10.1016/j.rse.2021.112317.
Glover, D.M., Doney, S.C., Oestreich, W.K., Tullo, A.W., 2018. Geostatistical analysis of mesoscale spatial variability and error in SeaWiFS and MODIS/aqua global ocean color data. J. Geophys. Res. Oceans 123, 22–39. https://doi.org/10.1002/2017JC013023.
Graban, S., Dall'Olmo, G., Goult, S., Sauzède, R., 2020. Accurate deep-learning estimation of chlorophyll-a concentration from the spectral particulate beam-attenuation coefficient. Opt. Express 28, 24214–24228. https://doi.org/10.1364/OE.397863.
Gregg, W.W., Rousseaux, C.S., Franz, B.A., 2017. Global trends in ocean phytoplankton: a new assessment using revised ocean colour data. Remote Sens. Lett. 8, 1102–1111. https://doi.org/10.1080/2150704X.2017.1354263.
Groom, S., Sathyendranath, S., Ban, Y., Bernard, S., Brewin, R., Brotas, V., Brockmann, C., Chauhan, P., Choi, J.K., Chuprin, A., Ciavatta, S., Cipollini, P., Donlon, C., Franz, B., He, X.Q., Hirata, T., Jackson, T., Kampel, M., Krasemann, H., Lavender, S., Pardo-Martinez, S., Melin, F., Platt, T., Santoleri, R., Skakala, J., Schaeffer, B., Smith, M., Steinmetz, F., Valente, A., Wang, M.H., 2019. Satellite Ocean colour: current status and future perspective. Front. Mar. Sci. 6 https://doi.org/10.3389/fmars.2019.00485.
Hlaing, S., Harmel, T., Gilerson, A., Foster, R., Weidemann, A., Arnone, R., Wang, M.H., Ahmed, S., 2013. Evaluation of the VIIRS Ocean color monitoring performance in coastal regions. Remote Sens. Environ. 139, 398–414. https://doi.org/10.1016/j.rse.2013.08.013.
Hooker, S.B., Lazin, G., Zibordi, G., McLean, S., 2002. An evaluation of above- and in-water methods for determining water-leaving radiances. J. Atmos. Ocean. Technol. 19, 486–515. https://doi.org/10.1175/1520-0426(2002)019<0486:AEOAAI>2.0.CO;2.
Hu, C.M., Le, C.F., 2014. Ocean color continuity from VIIRS measurements over Tampa Bay. IEEE Geosci. Remote Sens. Lett. 11, 945–949. https://doi.org/10.1109/LGRS.2013.2282599.
Hu, C.M., Lee, Z., Franz, B., 2012. Chlorophyll a algorithms for oligotrophic oceans: A novel approach based on three-band reflectance difference. J. Geophys. Res. Oceans 117. https://doi.org/10.1029/2011JC007395.
Hu, C.M., Feng, L., Lee, Z., 2013. Uncertainties of SeaWiFS and MODIS remote sensing reflectance: implications from clear water measurements. Remote Sens. Environ. 133, 168–182. https://doi.org/10.1016/j.rse.2013.02.012.
Hu, C.M., Barnes, B.B., Qi, L., Corcoran, A.A., 2015. A harmful algal bloom of Karenia brevis in the northeastern Gulf of Mexico as revealed by MODIS and VIIRS: a comparison. Sensors 15, 2873–2887. https://doi.org/10.3390/s150202873.
Hu, C.M., Feng, L., Lee, Z.P., Franz, B.A., Bailey, S.W., Werdell, P.J., Proctor, C.W., 2019. Improving satellite global chlorophyll a data products through algorithm refinement and data recovery. J. Geophys. Res. Oceans 124, 1524–1543. https://doi.org/10.1029/2019JC014941.
IOCCG, 2018. Inherent Optical Property Measurements and Protocols: Absorption Coefficient. IOCCGISO, Dartmouth, NS, Canada (2008). Guide to the Expression of Uncertainty in Measurement. Joint Committee for Guides in Metrology–JCGM 100. 2008 (ISO/IEC Guide 98–3). http://www.iso.org/sites/JCGM/GUM-introduction.htm.
ISO, 2008. Guide to the Expression of Uncertainty in Measurement.. Joint Committee for Guides. ISO/IEC Guide 98–3, http://www.iso.org/sites/JCGM/GUM-introduction.htm in Metrology, 100.
Jeffrey, S.W., Mantoura, R.F.C., Wright, S.W., 1997. Phytoplankton Pigments in Oceanography. UNESCO, Paris.
Kahru, M., Kudela, R.M., Anderson, C.R., Mitchell, B.G., 2015. Optimized merger of ocean chlorophyll algorithms of MODIS-aqua and VIIRS. IEEE Geosci. Remote Sens. Lett. 12, 2282–2285. https://doi.org/10.1109/LGRS.2015.2470250.
Koponen, S., Attila, J., Pulliainen, J., Kallio, K., Pyhalahti, T., Lindfors, A., Rasmus, K., Hallikainen, M., 2007. A case study of airborne and satellite remote sensing of a spring bloom event in the Gulf of Finland. Cont. Shelf Res. 27, 228–244. https://doi.org/10.1016/j.csr.2006.10.006.
Kratzer, S., Plowey, M., 2021. Integrating mooring and ship-based data for improved validation of OLCI chlorophyll-a products in the Baltic Sea. Int. J. Appl. Earth Obs. Geoinf. 94, 102212. https://doi.org/10.1016/j.jag.2020.102212.
Lee, Shang, S., Hu, C., Lewis, M., Amone, R., Li, Y., Lubac, B., 2010. Time series of bio-optical properties in a subtropical gyre: Implications for the evaluation of interannual trends of biogeochemical properties. J. Geophys. Res., Oceans 115 (C09012). https://doi.org/10.1029/2009JC005865.
Li, J., Jamet, C., Zhu, J.H., Han, B., Li, T.J., Yang, A.N., Guo, K., Jia, D., 2019. Error budget in the validation of radiometric products derived from OLCI around the China Sea from Open Ocean to coastal waters compared with MODIS and VIIRS. Remote Sens. 11. https://doi.org/10.3390/rs11202400.
Liu, Y.Y., Rottgers, R., Ramirez-Perez, M., Dinter, T., Steinmetz, F., Nothig, E.M., Hellmann, S., Wiegmann, S., Bracher, A., 2018. Underway spectrophotometry in the Fram Strait (European Arctic Ocean): a highly resolved chlorophyll a data source for complementing satellite ocean color. Opt. Express 26, A678–A696. https://doi.org/10.3390/rs11030318.
Liu, B., D'Sa, E.J., Maiti, K., Rivera-Monroy, V.H., Xue, Z., 2021. Biogeographical trends in phytoplankton community size structure using adaptive sentinel 3-OLCI chlorophyll a and spectral empirical orthogonal functions in the estuarine-shelf waters of the northern Gulf of Mexico. Remote Sens. Environ. 252, 112154. https://doi.org/10.1016/j.rse.2020.112154.
Loisel, H., Morel, A., 1998. Light scattering and chlorophyll concentration in case 1 waters: a re-examination. Limnol. Oceanogr. 43, 847–857. https://doi.org/10.4319/lo.1998.43.5.0847.
Loisel, H., Stramski, D., Dessailly, D., Jamet, C., Li, L.H., Reynolds, R.A., 2018. An inverse model for estimating the optical absorption and backscattering coefficients of seawater from remote-sensing reflectance over a broad range of oceanic and coastal marine environments. J. Geophys. Res. Oceans 123, 2141–2171. https://doi.org/10.1002/2017JC013632.
Longhurst, A., Sathyendranath, S., Platt, T., Caverhill, C., 1995. An estimate of global primary production in the ocean from satellite radiometer data. J. Plankton Res. 17 (6), 1245–1271. https://doi.org/10.1093/plankt/17.6.1245.
Martinez, E., Antoine, D., D'Ortenzio, F., Gentili, B., 2009. Climate-driven basin-scale decadal oscillations of oceanic phytoplankton. Science 326, 1253–1256. https://doi.org/10.1126/science.1177012.
Mazeran, C., Brockmann, C., Ruescas, A., Steinmetz, F., 2020. ESA Ocean Colour Climate Change Initiative – Phase 3: System Vicarious Calibration of SeaWiFS, MODIS, MERIS and VIIRS Sensors Processed by POLYMER. Report D 2.1. European Space Agency, ESRIN, Italy.
McClain, C.R., Feldman, G.C., Hooker, S.B., 2004. An overview of the SeaWiFS project and strategies for producing a climate research quality global ocean bio-optical time series. Deep-Sea Res. Part II-Top. Stud. Oceanogr. 51, 5–42. https://doi.org/10.1016/j.rse.2013.03.025.
Meister, G., Franz, B.A., 2014. Corrections to the MODIS aqua calibration derived from MODIS Aqua Ocean color products. IEEE Trans. Geosci. Remote Sens. 52, 6534–6541. https://doi.org/10.1109/TGRS.2013.2297233.
Meister, G., McClain, C.R., 2010. Point-spread function of the ocean color bands of the moderate resolution imaging spectroradiometer on aqua. Appl. Opt. 49, 6276–6285. https://doi.org/10.1364/AO.49.006276.
Meister, G., Franz, B.A., Kwiatkowska, E.J., McClain, C.R., 2012. Corrections to the calibration of MODIS Aqua Ocean color bands derived from SeaWiFS data. IEEE Trans. Geosci. Remote Sens. 50, 310–319. https://doi.org/10.1109/TGRS.2011.2160552.
Mélin, F., Franz, B.A., 2014. Assessment of satellite ocean colour radiometry and derived geophysical products, in optical radiometry for oceans climate measurements, chap. 6.1. In: Zibordi, G., Donlon, C., Parr, A. (Eds.), Experimental Methods in the Physical Sciences, 47, pp. 609–638. https://doi.org/10.1016/B978-0-12-417011-7.00020-9.
Mélin, F., Sclep, G., Jackson, A., Sathyendranath, S., 2016. Uncertainty estimates of remote sensing reflectance derived from comparison of ocean color satellite data sets. Remote Sens. Environ. 177, 107–124. https://doi.org/10.1016/j.rse.2016.02.014.
Mobley, C.D., 1999. Estimation of the remote sensing reflectance from above-surface measurements. Appl. Opt. 38, 7442–7455. https://doi.org/10.1364/AO.38.007442.
Mograne, M.A., Jamet, C., Loisel, H., Vantrepotte, V., Meriaux, X., Cauvin, A., 2019. Evaluation of five atmospheric correction algorithms over french optically-complex waters for the sentinel-3A OLCI Ocean color sensor. Remote Sens. 11 https://doi.org/10.3390/rs11060668.
Moore, T.S., Campbell, J.W., Dowell, M.D., 2009. A class-based approach to characterizing and mapping the uncertainty of the MODIS Ocean chlorophyll

product. Remote Sens. Environ. 113, 2424–2430. https://doi.org/10.1016/j.rse.2009.07.016.
Moore, T.S., Campbell, J.W., Feng, H., 2015. Characterizing the uncertainties in spectral remote sensing reflectance for SeaWiFS and MODIS-aqua based on global in situ matchup data sets. Remote Sens. Environ. 159, 14–27. https://doi.org/10.1016/j.rse.2014.11.025.
Moore, G., Mazeran, C., Huot, J.-P., 2017. MERIS Algorithm Theoretical Basis Document 2.6: Case II.S Bright Pixel Atmospheric Correction. European Space Agency.
Morel, A., 1988. Optical modeling of the upper ocean in relation to its biogenous matter content (case I waters). J. Geophys. Res. Oceans 93, 10749–10768. https://doi.org/10.1029/JC093iC09p10749.
Morel, A., Antoine, D., 2011. Pigment index retrieval in case 1 waters. In: Algorithm Technical Baseline Document 2.9. European Space Agency.
Morel, A., Maritorena, S., 2001. Bio-optical properties of oceanic waters: a reappraisal. J. Geophys. Res. Oceans 106, 7163–7180. https://doi.org/10.1029/2000JC000319.
Mueller, J.L.E.A., 2000. Above-water radiance and remote sensing reflectance measurements and analysis protocols. In: Fargion, G.S., Mueller, J.L. (Eds.), Ocean Optics Protocols for Satellite Ocean Color Sensor Validation. National Aeronautical and Space Administration, Washingotn, USA.
Muller, D., Krasemann, H., Brewin, R.J.W., Brockmann, C., Deschamps, P.Y., Doerffer, R., Fomferra, N., Franz, B.A., Grant, M.G., Groom, S.B., Melin, F., Platt, T., Regner, P., Sathyendranath, S., Steinmetz, F., Swinton, J., 2015. The ocean colour climate change initiative: II. Spatial and temporal homogeneity of satellite data retrieval due to systematic effects in atmospheric correction processors. Remote Sens. Environ. 162, 257–270. https://doi.org/10.1016/j.rse.2015.01.033.
O'Reilly, J.E., et al., 2000. Ocean color chlorophyll-a algorithms for SeaWiFS, OC2 and OC4. In: Hooker, S.B., Firestone, E.R. (Eds.), SeaWiFS Postlaunch Calibration and Validation Analyses: Part 3. NASA Goddard Space Flight Center, Greenbelt: Greenbelt, MD, pp. 9–23.
O'Reilly, J.E., Maritorena, S., Mitchell, B.G., Siegel, D.A., Carder, K.L., Garver, S.A., Kahru, M., McClain, C., 1998. Ocean color chlorophyll algorithms for SeaWiFS. J. Geophys. Res. Oceans 103, 24937–24953. https://doi.org/10.1029/98JC02160.
Pitarch, J., Volpe, G., Colella, S., Krasemann, H., Santoleri, R., 2016. Remote sensing of chlorophyll in the Baltic Sea at basin scale from 1997 to 2012 using merged multi-sensor data. Ocean Sci. 12, 379–389. https://doi.org/10.5194/os-12-379-2016.
Siegel, D.A., Franz, B.A., 2010. OCEANOGRAPHY century of phytoplankton change. Nature 466. https://doi.org/10.1038/466569a (569−+).
Siegel, D.A., Buesseler, K.O., Doney, S.C., Sailley, S.F., Behrenfeld, M.J., Boyd, P.W., 2014. Global assessment of ocean carbon export by combining satellite observations and food-web models. Glob. Biogeochem. Cycles 28, 181–196. https://doi.org/10.1002/2013GB004743.
Slade, W.H., Boss, E., Dall'Olmo, G., Langner, M.R., Loftin, J., Behrenfeld, M.J., Roesler, C., Westberry, T.K., 2010. Underway and moored methods for improving accuracy in measurement of spectral particulate absorption and attenuation. J. Atmos. Ocean. Technol. 27, 1733–1746. https://doi.org/10.1175/2010JTECHO755.1.
Steinmetz, F., Ramon, D., 2018. Sentinel-2 MSI and Sentinel-3 OLCI consistent ocean colour products using POLYMER. In: Frouin, R.J., Murakami, H. (Eds.), Remote Sensing of the Open and Coastal Ocean and Inland Waters.
Steinmetz, F., Deschamps, P.Y., Ramon, D., 2011. Atmospheric correction in presence of sun glint: application to MERIS. Opt. Express 19, 9783–9800. https://doi.org/10.1364/OE.19.009783.
Stock, A., Subramaniam, A., 2020. Accuracy of empirical satellite algorithms for mapping phytoplankton diagnostic pigments in the Open Ocean: a supervised learning perspective. Front. Mar. Sci. 7, 599. https://doi.org/10.3389/fmars.2020.00599.
Stramska, M., Petelski, T., 2003. Observations of oceanic whitecaps in the north polar waters of the Atlantic. J. Geophys. Res. Oceans 108 (C3), 3086. https://doi.org/10.1029/2002JC001321.
Szeto, M., Werdell, P.J., Moore, T.S., Campbell, J.W., 2011. Are the world's oceans optically different? J. Geophys. Res. Oceans 116. https://doi.org/10.1029/2011JC007230.
Tan, J, Frouin, R., Ramon, D., Steinmetz, F., 2019. On the Adequacy of Representing Water Reflectance by Semi-Analytical Models in Ocean Color Remote Sensing. Remote Sens. 11 (23), 2820 https://doi.org/10.3390/rs11232820.
Tilstone, G., Dall'Olmo, G., Hieronymi, M., Ruddick, K., Beck, M., Ligi, M., Costa, M., D'Alimonte, D., Vellucci, V., Vansteenwegen, D., Bracher, A., Wiegmann, S., Kuusk, J., Vabson, V., Ansko, I., Vendt, R., Donlon, C., Casal, T., 2020. Field intercomparison of radiometer measurements for ocean colour validation. Remote Sens. 12 https://doi.org/10.3390/rs12101587.
Uprety, S., Cao, C.Y., Xiong, X.X., Blonski, S., Wu, A.S., Shao, X., 2013. Radiometric intercomparison between Suomi-NPP VIIRS and aqua MODIS reflective solar bands using simultaneous nadir overpass in the low latitudes. J. Atmos. Ocean. Technol. 30, 2720–2736. https://doi.org/10.1175/JTECH-D-13-00071.1.
Volpe, G., Santoleri, R., Vellucci, V., d'Alcala, M.R., Marullo, S., D'Ortenzio, F., 2007. The colour of the Mediterranean Sea: global versus regional bio-optical algorithms evaluation and implication for satellite chlorophyll estimates. Remote Sens. Environ. 107, 625–638. https://doi.org/10.1016/j.rse.2006.10.017.
Wang, M.H., Shi, W., 2006. Cloud masking for ocean color data processing in the coastal regions. IEEE Trans. Geosci. Remote Sens. 44 (11) https://doi.org/10.1109/TGRS.2006.876293, 3196–3105.
Wang, M.H., Son, S., 2016. VIIRS-derived chlorophyll-a using the ocean color index method. Remote Sens. Environ. 182, 141–149. https://doi.org/10.1016/j.rse.2016.05.001.
Wang, M.H., Son, S., Shi, W., 2009. Evaluation of MODIS SWIR and NIR-SWIR atmospheric correction algorithms using SeaBASS data. Remote Sens. Environ. 113, 635–644. https://doi.org/10.1016/j.rse.2008.11.005.
Werdell, P.J., Bailey, S.W., 2005. An improved in-situ bio-optical data set for ocean color algorithm development and satellite data product validation. Remote Sens. Environ. 98, 122–140. https://doi.org/10.1016/j.rse.2005.07.001.
Werdell, P.J., McKinna, L.I.W., Boss, E., Ackleson, S.G., Craig, S.E., Gregg, W.W., Lee, Z., Maritorena, S., Roesler, C.S., Rousseaux, C.S., Stramski, D., Sullivan, J.M., Twardowski, M.S., Tzortziou, M., Zhang, X.D., 2018. An overview of approaches and challenges for retrieving marine inherent optical properties from ocean color remote sensing. Prog. Oceanogr. 160, 186–212. https://doi.org/10.1016/j.pocean.2018.01.001.
Westberry, T.K., Dall'Olmo, G., Boss, E., Behrenfeld, M.J., Moutin, T., 2010. Coherence of particulate beam attenuation and backscattering coefficients in diverse open ocean environments. Opt. Express 18, 15419–15425. https://doi.org/10.1364/OE.18.015419.
Zibordi, Zibordi, Z., Mélin, F., Voss, K.J., Johnson, B.C., Franz, B.A., Kwiatkowska, E., Huot, J.P., Wang, M., Antoine, D., 2015. System Vicarious Calibration for Ocean Color Climate Change Applications: Requirements for In Situ Data. Remote Sens. Environ. 159, 361–369. https://doi.org/10.1016/j.rse.2014.12.015.
Zibordi, G., Berthon, J.F., Melin, F., D'Alimonte, D., 2011. Cross-site consistent in situ measurements for satellite ocean color applications: the BiOMaP radiometric dataset. Remote Sens. Environ. 115, 2104–2115. https://doi.org/10.1016/j.rse.2011.04.013.
Zibordi, G., Melin, F., Berthon, J.F., 2018. A regional assessment of OLCI data products. IEEE Geosci. Remote Sens. Lett. 15, 1490–1494. https://doi.org/10.1109/LGRS.2018.2849329.